The Astrophysical Journal, 972:192 (20pp), 2024 September 10 https://doi.org/10.3847/1538-4357/ad5f8b

The Most Sensitive Radio Recombination Line Measurements Ever Made of the Galactic Warm Ionized Medium

T. M. Bania[1], Dana S. Balser[2], Trey V. Wenger[3], Spencer J. Ireland[1,4], L. D. Anderson[5,6,7], and Matteo Luisi[6,8]
[1] Institute for Astrophysical Research, Astronomy Department, Boston University, 725 Commonwealth Avenue, Boston, MA 02215, USA; bania@bu.edu
[2] National Radio Astronomy Observatory, 520 Edgemont Road, Charlottesville, VA 22903, USA
[3] NSF Astronomy & Astrophysics Postdoctoral Fellow, Department of Astronomy, University of Wisconsin–Madison, Madison, WI 53706, USA
[4] Department of Physics, New Mexico Tech, Socorro, NM 87801, USA
[5] Department of Physics and Astronomy, West Virginia University, Morgantown, WV 26506, USA
[6] Center for Gravitational Waves and Cosmology, West Virginia University, Chestnut Ridge Research Building, Morgantown, WV 26505, USA
[7] Green Bank Observatory, P.O. Box 2, Green Bank, WV 24944, USA
[8] Department of Physics, Westminster College, New Wilmington, PA 16172, USA
Received 2023 December 24; revised 2024 June 27; accepted 2024 July 3; published 2024 September 9

Abstract

Diffuse ionized gas pervades the disk of the Milky Way. We detect extremely faint emission from this Galactic warm ionized medium (WIM) using the Green Bank Telescope to make radio recombination line (RRL) observations toward two Milky Way sight lines: G20, $(\ell, b) = (20°, 0°)$, and G45, $(\ell, b) = (45°, 0°)$. We stack 18 consecutive Hnα transitions between 4.3 and 7.1 GHz to derive $\langle \mathrm{Hn}\alpha \rangle$ spectra that are sensitive to RRL emission from plasmas with emission measures EM $\gtrsim 10\,\mathrm{cm}^{-6}$ pc. Each sight line has two Gaussian-shaped spectral components with emission measures that range between ∼100 and ∼300 cm^{-6} pc. Because there is no detectable RRL emission at negative LSR velocities, the emitting plasma must be located interior to the solar orbit. The G20 and G45 emission measures imply rms densities of 0.15 and 0.18 cm^{-3}, respectively, if these sight lines are filled with homogeneous plasma. The observed $\langle \mathrm{Hn}\beta \rangle / \langle \mathrm{Hn}\alpha \rangle$ line ratios are consistent with LTE excitation for the strongest components. The high-velocity component of G20 has a narrow line width, 13.5 km s^{-1}, that sets an upper limit of $\lesssim$4000 K for the plasma electron temperature. This is inconsistent with the ansatz of a canonically pervasive, low-density, ∼10,000 K WIM plasma.

Unified Astronomy Thesaurus concepts: Interstellar line emission (844); Milky Way disk (1050); Radio spectroscopy (1359); Warm ionized medium (1788)

1. The Milky Way Warm Ionized Medium

Hoyle & Ellis (1963) were the first to suggest the existence of a layer of ionized gas along the Galactic plane with an electron density of ∼0.1 cm^{-3} and an electron temperature of $\sim 10^4$ K. This was based on their Hobart, Tasmania discovery of free–free absorption at frequencies less than 10 MHz against the synchrotron background observed at very low radio frequencies (Reber & Ellis 1956; Ellis et al. 1962). They estimated that the ionizing radiation necessary to produce the observed free–free absorption was consistent with flux from OB stars. The dispersion of radio waves from pulsars (Tanenbaum et al. 1968) and the observation of optical emission lines (Reynolds et al. 1973) from the interstellar medium (ISM) confirmed the existence of a warm ionized medium (WIM) in the Milky Way. Detection of Hα emission from the diffuse ionized gas (DIG) in the edge-on spiral galaxy NGC 891 showed that other galaxies had similar warm plasmas (Dettmar 1990; Rand et al. 1990). Here, we follow the convention of using the term "WIM" to refer to the warm ionized medium in the Milky Way and "DIG" to refer to the diffuse ionized gas in external galaxies (Haffner et al. 2009).

The WIM has been extensively studied with optical emission lines. Hα maps of the Galaxy show emission from almost every direction (e.g., Dennison et al. 1998; Gaustad et al. 2001; Haffner et al. 2003) with a volume filling factor larger than 0.2 (Reynolds 1991a). Sensitive observations of two emission lines from nitrogen indicate that the WIM is about 2000 K warmer than H II regions (Reynolds et al. 2001). Models of escaping radiation from H II regions indicate a harder spectrum for photons capable of ionizing hydrogen but a suppression of He-ionizing photons (Wood & Mathis 2004), consistent with observations of helium in the WIM (e.g., Reynolds & Tufte 1995).

Although known for 60 yr now, a detailed understanding of the WIM's origin, distribution, and physical properties remains to be crafted. Because of attenuation by dust, studies of the WIM using Hα are mostly limited to regions near the Sun or at high Galactic latitudes. Moreover, the relatively low spatial and spectral resolution of most Hα surveys cannot separate emission from the WIM with that from discrete, OB-star excited H II regions. This is particularly a problem in the inner Galactic disk.

Two recent radio recombination line (RRL) surveys overcome these limitations. The Green Bank Telescope (GBT) Diffuse Ionized Gas Survey (GDIGS; Anderson et al. 2021) is a 4–8 GHz RRL survey of the Milky Way disk that probes the distribution and properties of the WIM in the inner Galaxy ($32.^\circ3 > \ell > -5°$, $|b| < 0.^\circ5$). GDIGS has an angular resolution of 2.′6 and a spectral resolution of 0.5 km s^{-1}. A complimentary survey was completed with the Five-hundred-meter Aperture Spherical Radio Telescope (FAST) using RRL transitions spanning frequencies between 1 and 1.5 GHz for the Galactic zone $55° > \ell > 33°$, $|b| < 2°$ (Hou et al. 2022). FAST has an angular resolution of 3′ and a spectral resolution of 2.2 km s^{-1}.

Both surveys employ line-stacking of multiple RRL transitions observed simultaneously to increase the signal-to-noise ratio.

Using GDIGS data, Luisi et al. (2020) created a WIM-only RRL map of the W43 star formation complex that is devoid of emission from H II regions. Employing an empirical model that only accounts for the H II region locations, angular sizes, and RRL intensities, they were able to reproduce the observed WIM emission (also see Belfiore et al. 2022). This supports the notion that UV photons leaking from the H II regions surrounding O and B-type stars are the primary source of the ionization of the WIM.

The main limitation of these new RRL surveys is sensitivity. For example, GDIGS is sensitive to emission measures, EM $\equiv \int n_e^2\, d\ell \gtrsim 1100\,\mathrm{cm}^{-6}\,\mathrm{pc}$, whereas most H$\alpha$ surveys are several orders of magnitude more sensitive. GDIGS detects RRL emission from most directions but not at all possible velocities where H I gas exists. This may just be a sensitivity issue. For example, the GDIGS spectrum toward G20 shows no RRL emission (see discussion below).

Here, we use the GBT to search for faint RRL emission from two first Galactic quadrant sight lines: G20 and G45. These directions, at $(\ell,\ b) = (20^\circ,\ 0^\circ)$, and $(\ell,\ b) = (45^\circ,\ 0^\circ)$, respectively, were chosen because they contain no detected discrete H II regions, show extremely weak radio continuum emission, and have infrared emission morphologies that do not indicate any incipient star formation. Any RRL emission detected for these lines of sight (LOSs) would thus stem from the WIM.

2. Observations and Data Analysis

Using the GBT, we made the RRL observations during a series of sessions held between 2020 June and August (project GBT/20A–483). Measurements were made using the *C*-band (4–8 GHz) receiver and the Versatile GBT Astronomical Spectrometer (VEGAS) back end. Full details of data acquisition protocols, VEGAS tuning configuration, and calibration are described in our GDIGS paper (Anderson et al. 2021). GDIGS survey data were acquired using On the Fly Mapping. Here, however, we employ total power position switching by observing an off source (Off) position for 6 minutes and then the target (On) position for 6 minutes, for a total time of 12 minutes per scan. The Off position lies well outside the Galactic plane because the WIM is expected to be distributed throughout the Galactic disk with a large volume filling factor. The Off position is offset from the On by $(\Delta\ell,\ \Delta b) = (0.^\circ0,\ -3.^\circ5)$.

We tuned VEGAS to 64 different frequencies with two orthogonal linear polarizations each. A single 12 minute Off/On spectral pair thus simultaneously produces 128 independent 8192 channel spectra, each spanning a 23.4375 MHz bandwidth. The VEGAS tuning consisted of an assortment of hydrogen RRL transitions that lie in the 4–8 GHz bandpass of the *C*-band receiver. These included $\alpha(\Delta n = 1)$, $\beta(\Delta n = 2)$, and $\gamma(\Delta n = 3)$ transitions, where n is the transition principal quantum number. For α RRL transitions, the frequency extremes of this tuning are H97α (7.09541 GHz rest frequency) and H115α (4.26814 GHz rest frequency). This large frequency range produces significant differences in the GBT beam size (the half-power beamwidth, HPBW) and spectral resolution. The beam size increases from 107″ for H97α to 177″ for H115α and the spectral velocity resolution decreases from 0.12 km s^{-1} per channel for H97α to 0.20 km s^{-1} per channel for H115α.

After acquisition, the telescope data were converted into SDFITS format and then ported to the `TMBIDL` single-dish data analysis software package (Bania et al. 2016). All subsequent data analysis reported here is done in the `TMBIDL` environment.

The intensity scale is determined by injecting signals from a noise diode into the signal path every other second during observations. The flux density scale is then established after data acquisition using observations of the quasar 3C 286, which is a primary flux calibrator. For the GBT at *C*-band frequencies, this quasar is a point source whose intensity has varied by less than 1% over decades (Ott et al. 1994; Peng et al. 2000). Because the GBT gain at *C* band is 2 K Jy^{-1} (Ghigo et al. 2001), the 3C 286 observations allow us to determine the noise diode fluxes. Overall, this procedure establishes the intensity scale of our spectra to ∼5% accuracy.

To maximize our spectral sensitivity, we derive, for each target sight line, a single RRL spectrum for each Δn transition, α, β, and γ. We do this by averaging together all of the observed, usable RRL transitions for a given Δn. We call this procedure "stacking," and the result of this averaging is a "stacked" spectrum: $\langle \mathrm{Hn}\alpha \rangle$, $\langle \mathrm{Hn}\beta \rangle$, and $\langle \mathrm{Hn}\gamma \rangle$. Properties of the RRL transitions we use to craft these stacked spectra are summarized in Appendix A.

Stacking is possible because RRLs involve high-n level transitions wherein adjacent n levels have nearly the same energy. For example, our usable α transitions span the range from H97α to H115α. In LTE, the expected RRL intensities would differ by a factor of ∼1.66 between these two transitions. The expected line profiles, and hence the spectral line widths, should, however, be similar for all of these transitions. Since the primary goal here is to detect RRL emission, all usable RRL transitions can therefore be averaged together to increase the signal-to-noise ratio, producing the $\langle \mathrm{Hn}\alpha \rangle$, $\langle \mathrm{Hn}\beta \rangle$, and $\langle \mathrm{Hn}\gamma \rangle$ stacked spectra.

Stacking is not a simple average of the different transitions weighted by their individual integration times and system temperatures, although of course that must be part of the procedure. Stacking must correct for several other effects: (1) each transition has a unique rest frequency and spectral velocity resolution; (2) each transition's spectrum has a slightly different center velocity due to our VEGAS tuning; and (3) only one of the RRL transitions is Doppler tracked due to the limitations of the GBT IF system hardware. Using the procedure described below, we have successfully stacked RRL spectra taken with the Arecibo telescope/"Interim Correlator" spectrometer (Roshi et al. 2005) as well as the GBT *X*-band receiver/ACS spectrometer (Balser 2006).

To derive the stacked spectra reported here, we: (1) inspect for each transition all of the individual OffOn total power pairs and eliminate bad data; (2) calculate for each transition an average spectrum weighted by integration time and system temperature; (3) establish a common spectral velocity resolution for each transition by using a $\sin(x)/x$ interpolation (Roshi et al. 2005) referenced to our poorest resolution, H97α, spectrum; (4) align all of the transitions in velocity referenced to the Doppler tracked H103α spectrum; and (5) obtain a stacked spectrum by averaging all of the individual transition spectra processed in this way weighted by integration time and system temperature.

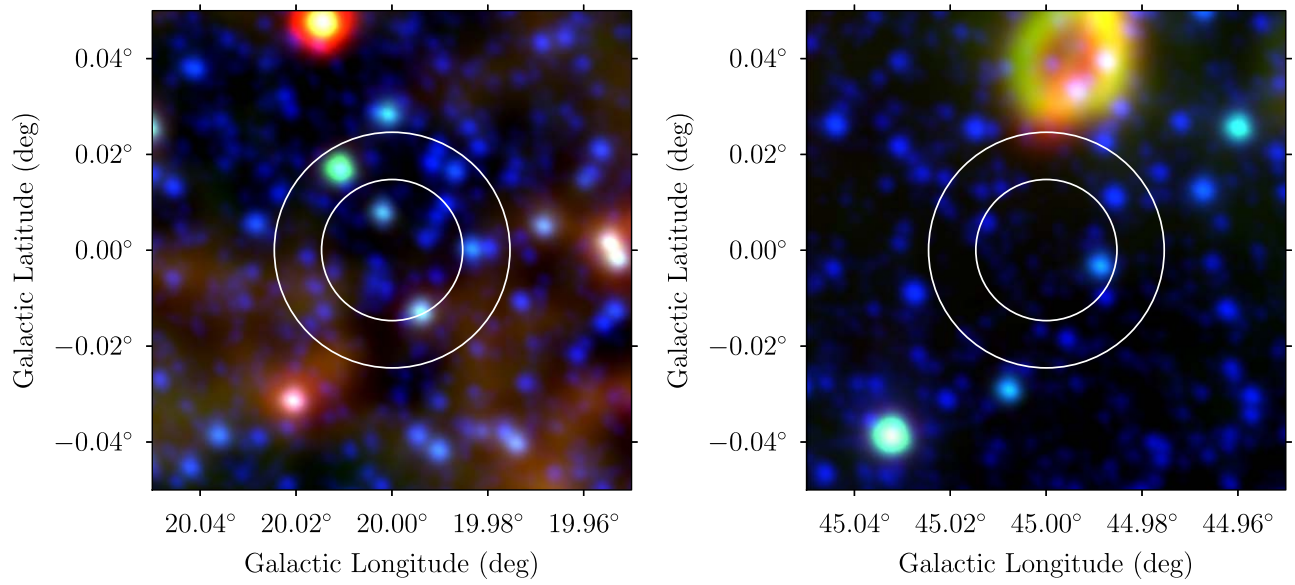

Figure 1. Mid-infrared WISE images of G20 (left) and G45 (right) where blue is 3.4 μm (stars), green 12 μm (emission from the photodissociation region; PDR), and red 22 μm (dust). The images are 6′ on a side. The circles show the range of the GBT beam size (HPBW) for this experiment, from 107″ for H97α to 177″ for H115α.

Table 1
Stacked Spectra Properties

Source	ℓ (deg)	b (deg)	Δn	# RRLs	$t_{\rm intg}$ (hr)	rms (mK)
G20	20.0	0.0	1: α	18	243.1	0.312
G20	...	...	2: β	22	302.4	0.288
G20	...	...	3: γ	7	91.0	0.483
G45	45.0	0.0	1: α	18	207.0	0.343
G45	...	...	2: β	22	270.8	0.314
G45	...	...	3: γ	7	79.6	0.518

The properties of the stacked spectra for the G20 and G45 sight lines are summarized in Table 1. Listed are the source name, the Galactic position, (ℓ, b), the RRL transition order, Δn, the number of transitions used to derive the stacked spectrum, the total integration time of the stacked spectrum, $t_{\rm intg}$, and the rms noise of the stacked spectrum after smoothing to 1 km s^{-1} resolution. The integration times for the $\langle$Hn$\alpha\rangle$ spectra exceed $\sim$200 hr and the spectral rms noise attained thereby is $\sim$300 μK. We believe these to be the most sensitive measurements of WIM RRL emission ever made.

3. RRL Emission from WIM Plasma

3.1. The G20 and G45 Lines of Sight

We detect weak RRL emission from both first Galactic quadrant sight lines: G20 and G45. Images of the mid-infrared emission seen toward these LOSs by the Wide-Field Infrared Survey Explorer (WISE; Wright et al. 2010) satellite are shown in Figure 1. There is clearly no extended IR emission in these directions consistent with either protostellar activity or high-mass star formation. Accordingly, the WISE Catalog of Galactic H II Regions (hereafter "The WISE Catalog"; Anderson et al. 2014) lists no OB-type star excited, discrete H II regions in these fields. (The doughnut-shaped object seen toward (ℓ, b) $\sim$ (44.99,+0.04) is a latent image from the overexposure of a saturated bright star located beyond the field of view shown in Figure 1).

The stacked $\langle$Hn$\alpha\rangle$ spectra we derive for G20 and G45 are shown in Figure 2. Both sight lines show two components of RRL emission from WIM plasma. In each direction, the higher LSR velocity component has the stronger peak intensity and narrower line width. The G20 components are twice as strong as their corresponding G45 components. We fit Gaussian functions to these components in order to quantify their spectral line properties. Table 2 compiles the results of these fits. Listed for each spectral component are the fit values and fit errors for the LSR velocity, $V_{\rm LSR}$, peak antenna temperature at the line center, $T_{\rm L}^{\rm A}$, the FWHM, line width, ΔV, the area under the component, $W_{\rm RRL}$, and an estimate of the emission measure, EM. The errors cited for peak intensity, line area, and emission measure include the 5% uncertainty in the intensity scale.

How do these spectra compare with the corresponding GDIGS and FAST measurements? Figure 3 shows that for G20, our deep integration is much more sensitive than GDIGS. GDIGS did not observe the G45 sight line but FAST did. FAST is more EM sensitive than GDIGS. Inspection of their Figure 5, however, also reveals no RRL emission. The strongest emission component that we measure toward either of our targets is therefore below the GDIGS and FAST sensitivity limits.

3.2. RRL Stacked Spectra

For both G20 and G45, RRL emission can be seen at nearly all LSR velocities between 0 km s^{-1} and the terminal velocity produced by Galactic rotation. The lack of any detected RRL emission at LSR velocities below 0 km s^{-1} means that in these directions, any RRL emission from WIM plasma located beyond the solar orbit about the Galactic Center must be below the sensitivity limits of our GBT observations.

We use the observed RRL emission components to estimate the emission measure. Assuming that the WIM plasma is extended and always fills the GBT beam, the brightness temperature at the line center of optically thin transitions in LTE, $T_{\rm L}^{\rm B}$, is (Gordon & Sorochenko 2002; Wilson et al. 2009, see their Equation (14.28) in the 5th edition; Wenger et al. 2019, see their Equation (16); and Anderson et al. 2021, see

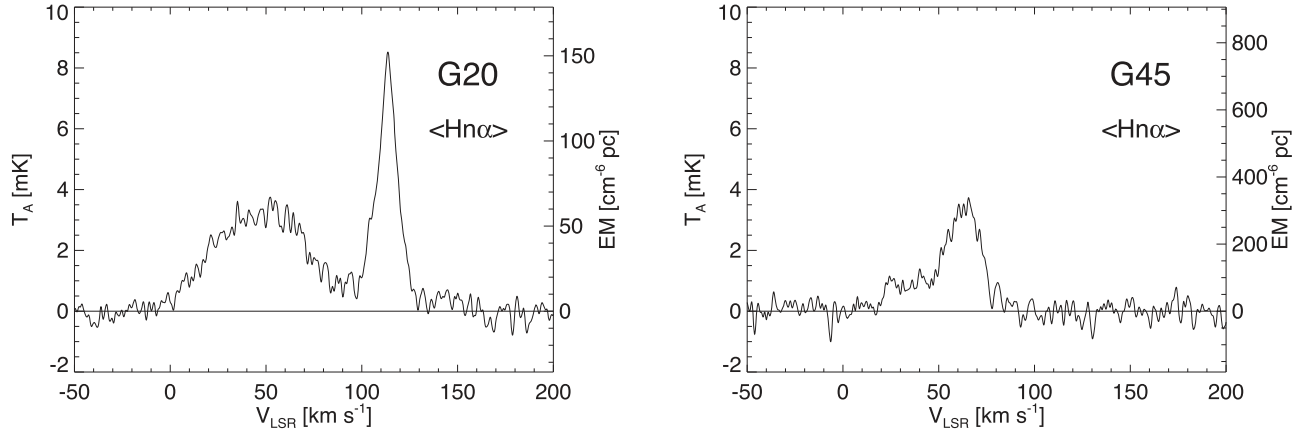

Figure 2. G20 and G45 stacked spectra for the $\langle \mathrm{Hn}\alpha \rangle$ transition. The spectra were smoothed to a 1 km s^{-1} velocity resolution, and the instrumental spectral baseline was subtracted. The emission measure, EM, axes stem from assumptions described in the text.

Table 2
$\langle \mathrm{Hn}\alpha \rangle$ Emission Properties

Source	$V_{\rm LSR}$ (km s^{-1})	$\sigma_{\rm LSR}$ (km s^{-1})	$T_{\rm L}^{\rm A}$ (mK)	$\sigma_{\rm L}$ (mK)	ΔV (km s^{-1})	$\sigma_{\Delta V}$ (km s^{-1})	$W_{\rm RRL}$ (mK km s^{-1})	$\sigma_{\rm W}$ (mK km s^{-1})	EM (cm^{-6} pc)	$\sigma_{\rm EM}$ (cm^{-6} pc)
G20	47.68	0.22	3.32	0.33	60.1	0.60	212.2	21.2	<245.5	24.5
G20	113.35	0.05	7.43	0.36	13.5	0.12	107.0	5.3	<123.8	6.2
G45	34.54	0.87	0.94	0.37	28.8	2.63	28.8	11.7	<112.4	45.7
G45	63.29	0.20	3.44	0.39	20.3	0.42	74.4	8.6	<290.3	33.5

their Equation (A4)):

$$\frac{T_{\rm L}^{\rm B}}{\rm K} = 3013\left(\frac{T_e}{\rm K}\right)^{-1.5}\left(\frac{\rm EM}{\rm cm^{-6}\,pc}\right)\left(\frac{\nu_0}{\rm GHz}\right)^{-1} \times \left(\frac{\Delta V}{\rm km\ s^{-1}}\right)^{-1}\left(\frac{\Delta n}{n}\right) f_{n+\Delta n,n} \quad (1)$$

where $T_{\rm e}$ is the plasma electron temperature, ν_0 is the rest frequency, and $f_{n+\Delta n,n}$ is the oscillator strength of the transition between $n+\Delta n$ and n. We consider only Hnα ($\Delta n = 1$) transitions and adopt the average rest frequency and oscillator strength of our $\langle \mathrm{Hn}\alpha \rangle$ stacked spectra. Using these values, Equation (1) yields for the emission measure:

$$\frac{\rm EM}{\rm cm^{-6}\,pc} = 4.57\left(\frac{T_e}{10^4\ \rm K}\right)^{1.5}\left(\frac{W_{\rm RRL}}{\rm mK\ km\ s^{-1}}\right). \quad (2)$$

Here, $W_{\rm RRL}$ [mK km s^{-1}], is the spectral area of an emission component. For a Gaussian line shape, $W_{\rm RRL} = 1.064\, T_{\rm L}^{\rm B}\, \Delta V$.

The RRL intensity values cited in all tables, however, list antenna temperature, $T_{\rm L}^{\rm A}$, the directly measured quantity, rather than the brightness temperature, $T_{\rm L}^{\rm B}$. Converting between antenna temperature to brightness temperature depends on the coupling between the characteristic angular size, $\Theta_{\rm WIM}$, of the RRL emitting plasma with the GBT beam. The stacked $\langle \mathrm{Hn}\alpha \rangle$ spectra stem from frequencies spanning the 4–8 GHz instantaneous bandwidth of the *C*-band receiver. For this experiment, the GBT HPBW beam size, $\Theta_{\rm BEAM}$, thus ranges between 177″ for H115α to 107″ for H97α. Here, we assume that the RRL emitting plasma is spatially extended and fills the GBT *C*-band beam(s): $\Theta_{\rm WIM} \gg \Theta_{\rm BEAM}$ always. For this case, the brightness temperature is $T_{\rm B} = T_{\rm A}/\eta_{\rm B}$ where the beam efficiency of the GBT at 5.7578 GHz is $\eta_{\rm B} = 0.93$ (Ghigo et al. 2001; Maddalena 2010; Balser et al. 2016).

Assuming an electron temperature and FWHM line width, the observed line antenna temperature, $T_{\rm L}^{\rm A}$, gives an EM of:

$$\frac{\rm EM}{\rm cm^{-6}\,pc} = 130.71\left(\frac{T_e}{10^4\ \rm K}\right)^{1.5}\left(\frac{\Delta V}{25\ \rm km\ s^{-1}}\right)\left(\frac{T_{\rm L}^{\rm A}}{\rm mK}\right). \quad (3)$$

Here, we use the line peak antenna temperature, $T_{\rm L}^{\rm A}$, for ease of interpreting the intensities shown in the spectra and listed in the tables. The needed conversion to brightness temperature has been absorbed into the numerical constant in Equation (3). The EM axes in Figures 2 and 3 and the values cited in Table 2 stem from Equation (3) using the observed $T_{\rm L}^{\rm A}$ and ΔV together with an assumed value for the plasma $T_{\rm e}$.

Although the electron temperature can be derived from the RRL line-to-continuum ratio, we did not measure the radio continuum for G20 and G45 and so cannot estimate $T_{\rm e}$ from our GBT observations. Studies of the WIM/DIG in the Milky Way and other galaxies using H$_\alpha$, [N II], [S II], and [O III] find that the electron temperature ranges between 6000 and 11,000 K (Haffner et al. 2009). Here, we use the observed line widths, ΔV, to constrain $T_{\rm e}$. Interpreting the observed line width as being due solely to thermal broadening, $\Delta V = \Delta V_{\rm th}$, sets a firm upper limit on the plasma electron temperature:

$$\frac{T_e}{\rm K} \leqslant 21.85\left(\frac{\Delta V}{\rm km\ s^{-1}}\right)^2 \quad (4)$$

where k is Boltzmann's constant, and $m_{\rm H}$ is the mass of hydrogen. The high LSR velocity RRL components seen toward G20 and G45 have the smallest line width for each sight line. These line widths give $T_{\rm e}$ upper limits of $\lesssim$4000 K and $\lesssim$9000 K for G20 and G45, respectively. These are the $T_{\rm e}$ values used for the EM axes in Figures 2 and 3 and for the EM values cited in Table 2.

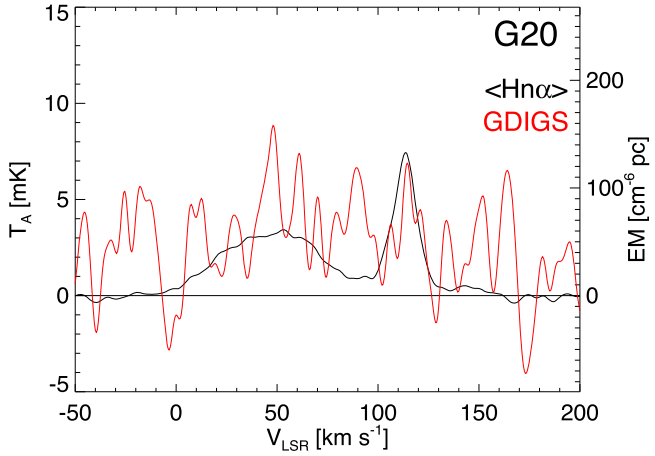

Figure 3. G20 $\langle \mathrm{Hn}\alpha \rangle$ spectrum (black) compared with the GDIGS spectral map pixel for the same direction (red). The $\langle \mathrm{Hn}\alpha \rangle$ data were smoothed to 5 km s^{-1} resolution. The $\sim$115 km s^{-1} $\langle \mathrm{Hn}\alpha \rangle$ component is below the GDIGS sensitivity limit.

The $\langle \mathrm{Hn}\alpha \rangle$ WIM spectra we derive for G20 and G45 are very deep integrations. The four $\langle \mathrm{Hn}\alpha \rangle$ emission components that we detect toward G20 and G45 yield emission measures ranging between $\sim$100 and $\sim$300 cm^{-6} pc (via Equation (2) and Table 2). All of these EM values stem from smoothing the native VEGAS velocity resolution per channel to 1 km s^{-1}. The rms noise cited in Table 1 is for this velocity resolution. The Figure 2 $\langle \mathrm{Hn}\alpha \rangle$ spectra are thus sensitive to emission measures EM $\gtrsim$ 20 cm^{-6} pc (the 3σ limit via Equation (3)). Below, when we consider LTE excitation or compare RRL models to our $\langle \mathrm{Hn}\alpha \rangle$ spectra, we smooth the per-channel velocity resolution to 5 km s^{-1}. At this resolution, these spectra have a 3σ sensitivity EM $\gtrsim$ 10 cm^{-6} pc. Nonetheless, even then, the spectra show no hint of additional emission components toward G20 and G45, especially at negative LSR velocities.

3.3. Properties of the Stacked Spectra

Before conducting further analyses of these stacked spectra, we explore how the RRL emission component line parameters vary as a function of frequency. After all, the stacked spectra are averages of many RRL transitions spanning a significant range of rest frequencies. To do this, we create "triad" spectra by stacking three consecutive Hnα RRL transitions together and smoothing the resulting spectrum to 5 km s^{-1} velocity resolution. Because our stacked $\langle \mathrm{Hn}\alpha \rangle$ spectra comprise 18 Hnα RRL transitions, there are six of these triad spectra for each sight line and they have rest frequencies spanning the entire bandwidth of the *C*-band receiver. These triad spectra have the sensitivity to enable Gaussian fits for three of the four RRL emission components present in our sight lines. Only the weaker, lower-velocity component of G45 cannot be analyzed this way.

This exploration is summarized in Figure 4 for G20 and Figure 5 for G45. These Figures show how the RRL emission component line parameters vary as a function of frequency. Filled symbols denote the high-velocity, stronger component; open symbols show the low-velocity, weaker component. For clarity, in these plots the frequency of these components has been dithered by $\pm$30 MHz. Horizontal lines flag the component parameters derived from Gaussian fits to the $\langle \mathrm{Hn}\alpha \rangle$ spectrum (Table 2).

The triad analysis shown in these figures does not reveal any issues that might compromise the stacking process. Overall, the triad data are consistent with the Table 2 Gaussian fits to the stacked $\langle \mathrm{Hn}\alpha \rangle$ spectra. Furthermore, none of the RRL emission component FWHM line widths show any systematic change with frequency. The strongest G20 emission component does have a significant LSR velocity gradient as a function of frequency. This is probably due to the changing GBT beam size sampling different volumes of plasma. Neither the weaker G20 component nor the G45 sight-line component show any LSR velocity gradient.

For both sight lines, however, the triad component $T_{\mathrm{L}}^{\mathrm{A}}$ and W_{RRL} values exhibit significant trends with frequency. The curves shown for T_{pk} and W_{RRL} are not fits to the data, rather they are notional curves that show the ν^{-1} frequency dependence expected for plasma in LTE and a source that fills the telescope beam (see Equation (1)).

3.4. Are the G20 and G45 Plasmas in LTE?

Are the $\langle \mathrm{Hn}\alpha \rangle$, $\langle \mathrm{Hn}\beta \rangle$, and $\langle \mathrm{Hn}\gamma \rangle$ stacked spectra consistent with LTE excitation? Here, we summarize our analysis of this question. The quantum mechanical details are provided in Appendix B, where it is shown that for our stacked spectra, the expected LTE $\langle\beta\rangle/\langle\alpha\rangle$ and $\langle\gamma\rangle/\langle\alpha\rangle$ line intensity ratios should be 0.27565 and 0.10672, respectively (see Table B2). We assess whether LTE excitation holds for our targets in two ways: (1) we scale the $\langle \mathrm{Hn}\alpha \rangle$ spectrum by the Table B2 expected LTE ratios for $\langle\beta\rangle$ and $\langle\gamma\rangle$ RRLs and compare this in Figure 6 to our stacked $\langle \mathrm{Hn}\beta \rangle$ and $\langle \mathrm{Hn}\gamma \rangle$ spectra; and (2) we fit Gaussian functions to the RRL emission components found in the $\langle \mathrm{Hn}\alpha \rangle$, $\langle \mathrm{Hn}\beta \rangle$, and $\langle \mathrm{Hn}\gamma \rangle$ spectra and compare these in Table 3 with the expected LTE ratios. In both cases, all of the stacked spectra are smoothed to a velocity resolution of 5 km s^{-1} to improve spectral sensitivity.

The first assessment of LTE is shown in Figure 6 where the left-hand plots compare the $\langle \mathrm{Hn}\alpha \rangle$ and $\langle \mathrm{Hn}\beta \rangle$ spectra for G20 and G45 with the expected LTE $\langle \mathrm{Hn}\beta \rangle$ spectrum. The right-hand plots compare the $\langle \mathrm{Hn}\beta \rangle$ and $\langle \mathrm{Hn}\gamma \rangle$ spectra with the expected LTE intensities. Both sight lines show $\langle \mathrm{Hn}\beta \rangle$ RRL emission that is slightly stronger than what is predicted by LTE. Although the G45 $\sim$ 35 km s^{-1} component matches the LTE prediction, this $\langle \mathrm{Hn}\beta \rangle$ component is only a $\sim 1\sigma$ signal. Compared with the other transitions, the $\langle \mathrm{Hn}\gamma \rangle$ spectra are not very sensitive (see Table 3). Only the $\sim$ 50 km s^{-1} emission component for G20 has any hint of γ emission, and this is only a $\gtrsim 1.5\sigma$ signal. For all other $\langle \mathrm{Hn}\gamma \rangle$ components, we can only provide upper limits for the LTE ratio.

The second evaluation of LTE uses Gaussian fits to the individual emission components found in the stacked α, β, and γ spectra. To make the LTE assessment that is summarized in Table 3, we use the observed integrated intensity of each component, W_{RRL}. (The slight differences in the reported fits for α components that are seen when comparing Tables 2 and 3 stem from the different velocity resolutions of the $\langle \mathrm{Hn}\alpha \rangle$ spectra).

The "LTE?" column in Table 3 gives the ratio between the observed RRL transition ratios and the expected LTE ratio. In LTE, the value of this ratio of ratios would be unity. For the strongest WIM components—113.4 km s^{-1} for G20 and 63.3 km s^{-1} for G45—this ratio is 1.11 ± 0.11 and 1.08 ± 0.11, respectively. We thus find that, within the errors, our $\langle \mathrm{Hn}\beta \rangle / \langle \mathrm{Hn}\alpha \rangle$ ratios are consistent with LTE excitation for both of these emission components. The lower-velocity components in these directions, however, have $\langle \mathrm{Hn}\beta \rangle / \langle \mathrm{Hn}\alpha \rangle$

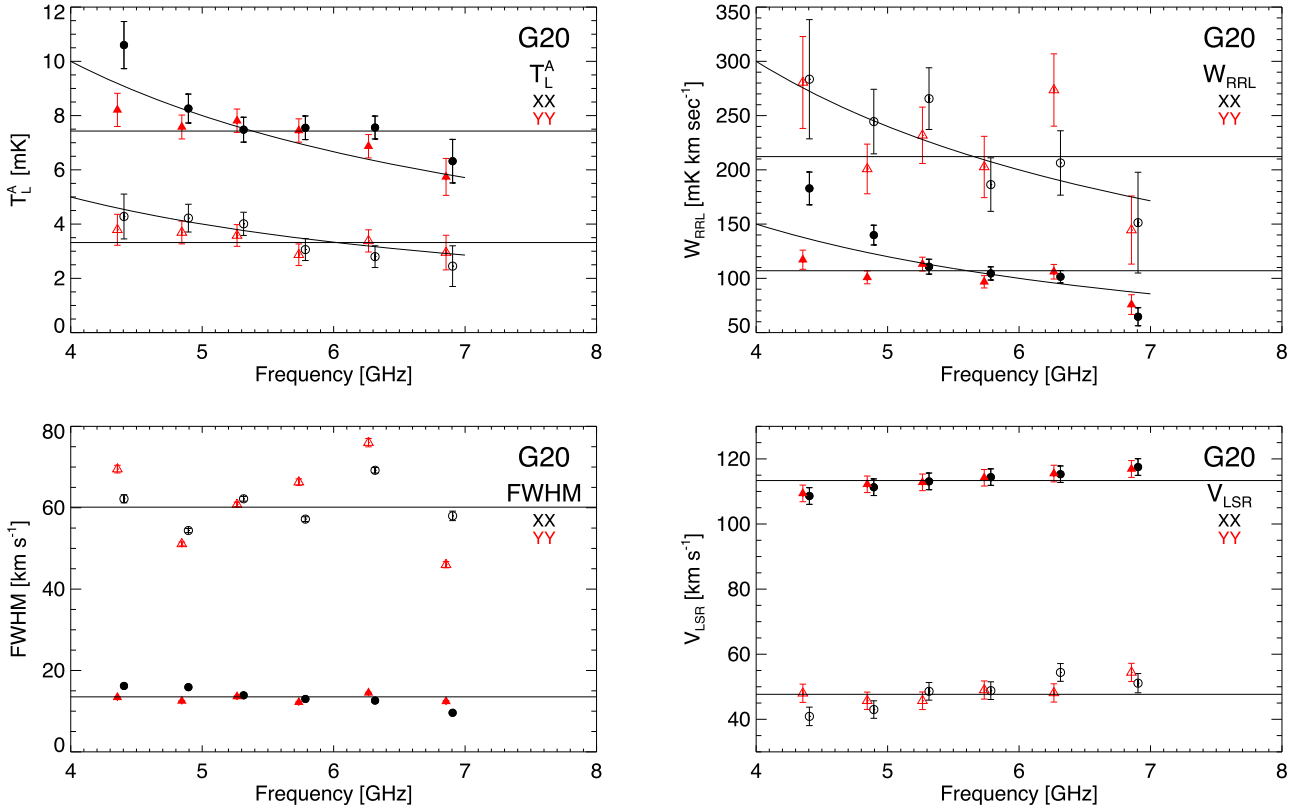

Figure 4. G20 sight-line RRL emission properties for spectral averages of three consecutive α transitions plotted as a function of frequency. Filled symbols denote the high-velocity, stronger component; open symbols show the low-velocity, weaker component. Horizontal lines flag the component parameters derived from Gaussian fits to the $\langle \mathrm{Hn}\alpha \rangle$ spectrum. The curves shown for T_{pk} and W_{RRL} are not fits to the data, rather they are notional curves that show the ν^{-1} frequency dependence expected for plasma in LTE and a source that fills the telescope beam (see the text).

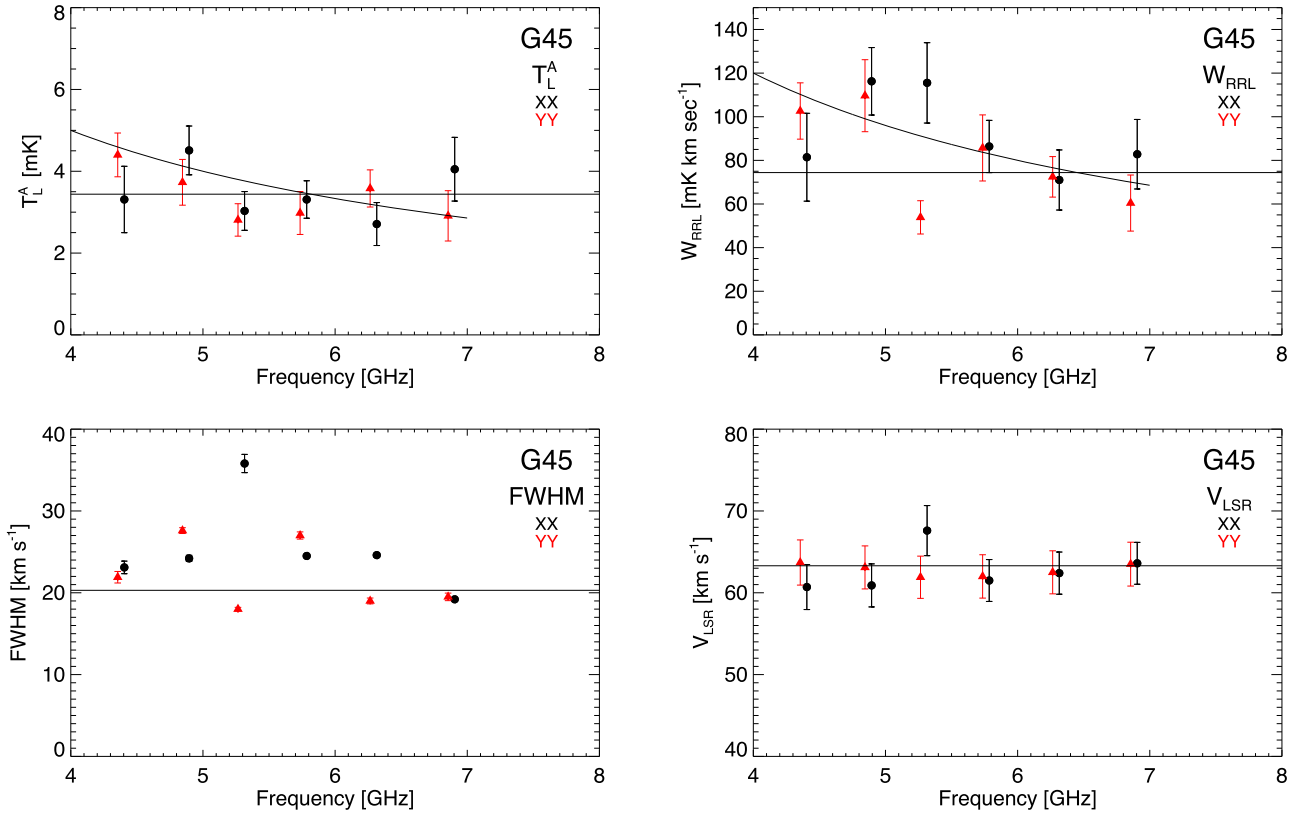

Figure 5. G45 sight-line RRL emission properties for spectral averages of three consecutive α transitions plotted as a function of frequency. Plot properties are the same as for Figure 4 except only one RRL component for this sight line at the higher $\sim$60 km s^{-1} velocity is strong enough to be analyzed in this manner.

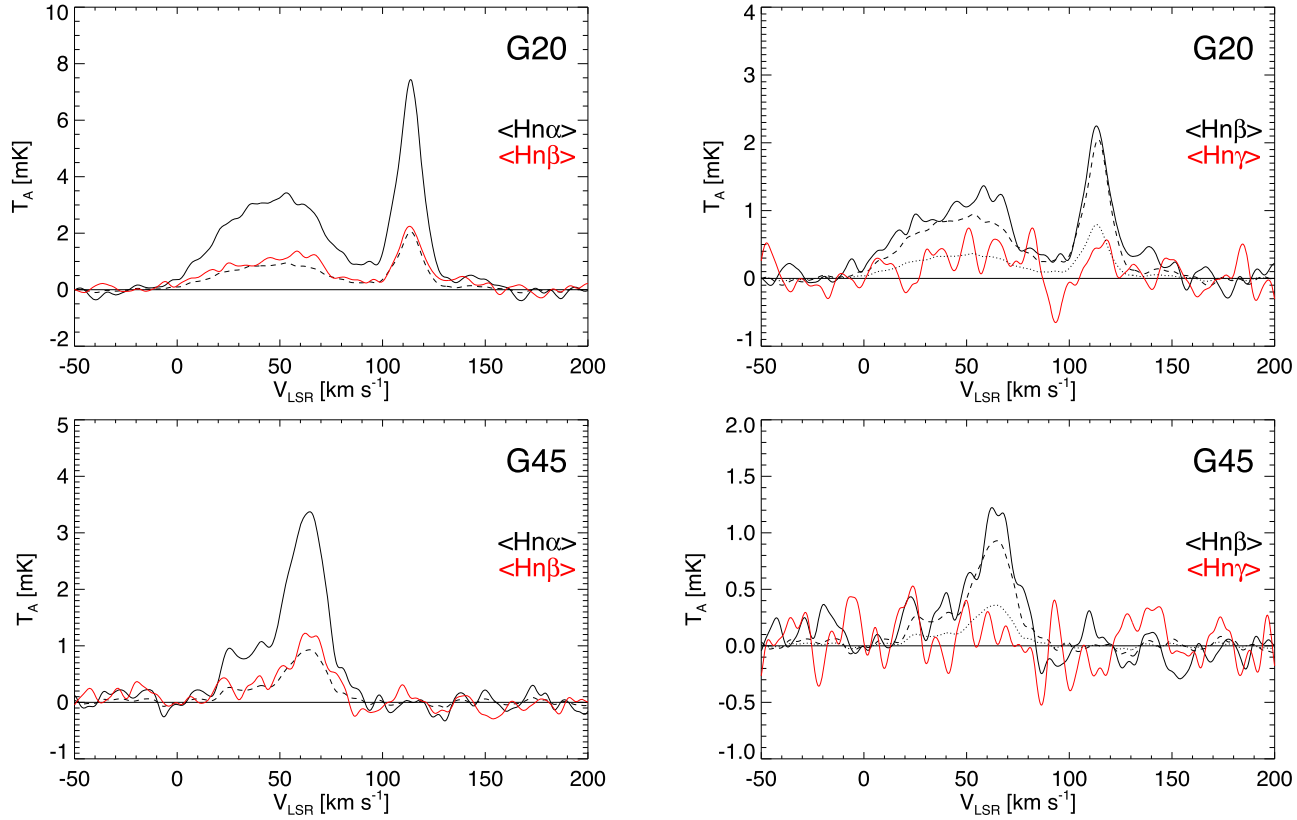

Figure 6. G20 and G45 stacked spectra for the $\langle \mathrm{Hn}\alpha \rangle$, $\langle \mathrm{Hn}\beta \rangle$, and $\langle \mathrm{Hn}\gamma \rangle$ transitions. The spectra have been smoothed to a 5 km s^{-1} velocity resolution. The left panels show the $\langle \mathrm{Hn}\alpha \rangle$ and $\langle \mathrm{Hn}\beta \rangle$ spectra. The dashed line spectrum is the expected LTE intensity of the β transition. The right panels show the $\langle \mathrm{Hn}\beta \rangle$ and $\langle \mathrm{Hn}\gamma \rangle$ spectra. The dashed and dotted spectra are the expected LTE intensities of the β and γ transitions, respectively.

Table 3
$\langle \mathrm{Hn}\alpha \rangle$, $\langle \mathrm{Hn}\beta \rangle$, and $\langle \mathrm{Hn}\gamma \rangle$ Emission Properties

Source	Δ n	$V_{\rm LSR}$	σ	$T_{\rm L}^{\rm A}$	σ	ΔV	σ	$W_{\rm RRL}$	σ	$W_{\rm RATIO}$ $\left(\frac{W(\Delta n)}{W(\alpha)}\right)$	σ	LTE?[a]	σ
		(km s^{-1})		(mK)		(km s^{-1})		(mK km s^{-1})					
G20	1: α	47.8	0.10	3.33	0.17	59.4	2.97	210.4	14.9	1.00	...	...	...
	2: β	48.5	0.21	1.17	0.06	62.4	3.12	77.8	5.5	0.37	0.04	1.34	0.13
	3: γ	55.3	0.74	0.74	0.37	42.0	2.10	33.1	16.6	0.16	0.08	1.48	0.75
G20	1: α	113.4	0.02	6.90	0.35	14.8	0.74	108.8	2.4	1.00	...	...	...
	2: β	113.7	0.06	2.11	0.11	14.8	0.74	33.3	2.4	0.31	0.03	1.11	0.11
	3: γ	115.8	0.33	<0.54	0.03	11.4	0.57	<6.5	...	<0.06	...	<0.56	...
G45	1: α	34.1	0.32	0.93	0.05	27.5	1.38	27.2	1.9	1.00	...	...	...
	2: β	37.6	2.34	0.32	0.02	42.8	6.41	14.6	2.3	0.54	0.09	1.95	0.34
	3: γ	...	...	<0.50	...	...	...	<14.9	...	<0.55	...	<5.14	...
G45	1: α	63.3	0.08	3.35	0.17	21.2	1.06	75.8	5.4	1.00	...	...	...
	2: β	65.3	0.18	1.09	0.02	19.4	1.16	22.5	1.8	0.30	0.03	1.08	0.11
	3: γ	...	...	<0.20	...	...	...	<4.5	...	<0.06	...	<0.56	...

Note.
[a] Ratio between observed $W_{\rm RATIO}$ and LTE ratio (Table B2); a plasma in LTE has value unity here.

ratios that are significantly larger than unity and thus are not consistent with LTE. Moreover, all ratios involving the $\langle \mathrm{Hn}\gamma \rangle$ spectra are compromised by the much poorer sensitivity of these spectra (see Appendix B).

3.5. WIM Ionization from Leakage Radiation?

WIM plasma halos envelope the PDRs that surround H II regions ionized by OB-type stars. Case studies of individual H II regions using RRL measurements, e.g., RCW 120 (Anderson et al. 2015) and NGC 7538 (Luisi et al. 2016), have found that WIM halos are produced by stellar UV photons leaking through the PDRs and that the fractions of the leaking radio continuum emission escaping into the WIM are ∼25% and ∼15%, respectively. Furthermore, optical Hα studies also suggest that if OB stars are the source of the WIM ionization, then the ISM OB-type star excited H II region distribution must allow at least ∼15%–25% of the H-ionizing Lyman continuum photons emitted by the stars to travel hundreds of parsecs within the Galactic disk (Reynolds 1991b).

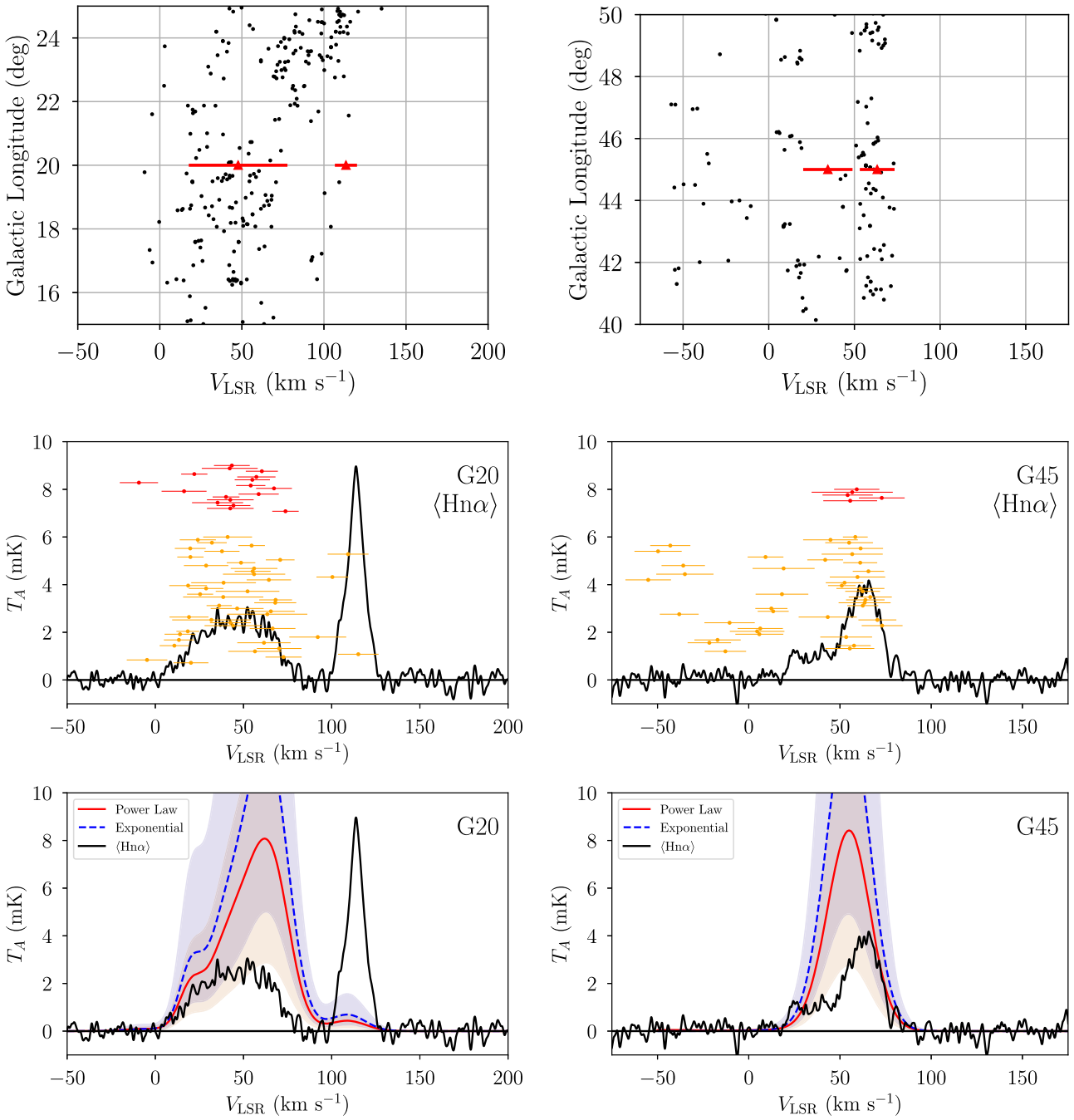

Figure 7. Comparison of G20 and G45 WIM emission with that from known Galactic H II regions. Top plots: (ℓ, v) distributions of OB-type-star excited H II regions near the G20 and G45 sight lines. Black circles are the LSR velocities of discrete H II regions. Red triangles and horizontal lines locate the LSR velocity and FWHM of the four RRL emission components we see toward G20 and G45. Middle plots: comparison of the stacked ⟨Hnα⟩ WIM spectra with Galactic H II regions. Shown are the RRL $V_{\rm LSR}$ and FWHM line widths of H II regions from the WISE Catalog plotted as a function of increasing angular separation of the nebular location from the G20 and G45 sight lines. The nearest H II region has the largest y-axis value. Red points are sources located within 30′ of each sight line; orange points are those located between 30′ and 100′. Bottom plots: predicted WIM emission due to diffuse ionized gas halos around H II regions. The solid red and dashed blue curves are the predictions of the Luisi et al. (2020) power-law and exponential models, respectively. The shaded regions represent the 95% confidence intervals.

Here, we assess whether the RRL emitting WIM plasma we find toward G20 and G45 is being ionized by leakage radiation from nearby, discrete H II regions. The Galactic context of our sight lines is provided by the top panels of Figure 7 which show the locations and LSR velocities of all known OB-type-star excited H II regions in the (ℓ, v) zone of the plots. Because we chose our targets to be devoid of obvious sources of ionizing radiation, as expected, neither sight line coincides in (ℓ, v)-space with any major concentration of H II regions. This is especially the case for the $\sim$115 km s^{-1} component of G20 and the $\sim$35 km s^{-1} component of G45: neither is located on the sky near any significant number of Galactic H II regions having their LSR velocities.

The middle panels of Figure 7 confirm that there are few Galactic H II regions that are near both in sky location and LSR velocity to the G20 $\sim$115 km s^{-1} and G45 $\sim$35 km s^{-1} RRL emission components. These plots show the $V_{\rm LSR}$ and FWHM of WISE Catalog H II regions that are located on the sky within

100′ of the G20 and G45 sight lines plotted as a function of increasing angular separation of the nebular location from the G20 and G45 sight lines.

The nearest H II region has the largest *y*-axis value. The remaining H II regions are plotted in separation sequence with the largest separation having the smallest *y*-axis value. (Other than providing a coordinate for plotting the angular separation *sequence*, these *y*-axis *values* have no physical meaning.) Red points in Figure 7 are sources located within 30′ of each sight line. There are 17 and 5 WISE Catalog H II regions located on the sky within 30′ of the G20 and G45 sight lines, respectively. Only three nebulae are within 10′ of our sight lines (two for G20 and one for G45) and the closest H II region lies 9′ from G45.

Some properties of these H II regions are compiled in Appendix Table C1. Listed for each nebula is the angular separation from the fiducial LOS, the IR radius, the Galactic (ℓ, b) position, the RRL parameters (RRL intensity, LSR velocity, and FWHM line width), together with the measurement errors. Again, the G20 $\sim$115 km s^{-1} and G45 $\sim$35 km s^{-1} components show very little (ℓ, v) correlation with known Galactic H II regions, and there are no H II regions at these velocities within 30′ of these sight lines.

Although there are few H II regions in close (ℓ, v) proximity to our sight lines, we may nonetheless be sensitive to extended WIM halos surrounding these nebulae. Luisi et al. (2020) developed empirical plasma halo models for the H II region complex W43. These models reproduce the observed RRL properties of maps of the WIM surrounding W43. The models assume that the WIM RRL intensity depends only on (1) the RRL intensity of nearby H II regions and (2) the angular distance to those H II regions from the fiducial LOS relative to the angular size of each nebula. For the W43 complex, they explored both an exponential and a power-law WIM emission distribution model, and they found that the power-law model is better able to reproduce the integrated WIM RRL intensity.

We apply the Luisi et al. (2020) models to our sight lines in order to explore the possibility that ionized halos around H II regions can explain the WIM emission in these directions. The bottom panels of Figure 7 show the predicted RRL emission due to WIM halos around all H II regions within 100′ of each sight line. The red solid lines show the power-law model prediction,

$$T_{A,\mathrm{model}} = k \sum_i T_{i,\mathrm{H\,II}} \left(\frac{r_i}{r_{i,\mathrm{H\,II}}} \right)^m, \tag{5}$$

and the blue dashed lines show the exponential model prediction,

$$T_{A,\mathrm{model}} = k \sum_i T_{i,\mathrm{H\,II}}\, \mathrm{e}^{-m(r_i/r_{i,\mathrm{H\,II}})}, \tag{6}$$

where $T_{i,\mathrm{H\,II}}$ is the H II region RRL spectrum, r_i is the angular separation between the sight line and the nominal H II region position, $r_{i,\mathrm{H\,II}}$ is the angular IR radius of the H II region, and k and m are the free parameters. The H II region RRL spectrum is evaluated from the RRL parameters in Appendix Table C1. The sum is taken over all H II regions within 100′ of each sight line for which there is an RRL intensity measurement listed in the Table. We adopt $k = 0.28 \pm 0.08$ and $m = -1.85 \pm 0.12$ for the power-law model and $k = 0.15 \pm 0.04$ and $m = 0.33 \pm 0.05$ for the exponential model as determined by Luisi et al. (2020) for the W43 complex.

We note, however, two important differences between our analysis and that of Luisi et al. (2020): (1) they fit their model to the integrated RRL intensity rather than the RRL spectra, and (2) they parameterize their model in terms of the average integrated RRL intensity over the H II region rather than the "peak" RRL spectrum at the nominal H II region position. For nebulae comparable in size to the telescope beam, the "peak" intensity is equal to the average intensity, but for angularly large nebulae, the difference will depend on the emission morphology. The shaded regions in the bottom panels of Figure 7 represent the 95% confidence intervals determined by Monte Carlo resampling the H II region RRL parameters and the model parameters k and m.

These empirical models, fit to the W43 complex, may not be applicable to every Galactic H II region. By applying such models here, we inherently assume that the relative distribution of WIM emission around every H II region is the same as that around nebulae in the W43 complex. Luisi et al. (2019) found significant variations in the radial distribution of RRL emission around several H II regions. The magnitude of this variation is far greater than the statistical uncertainties shown in the bottom panels of Figure 7. Furthermore, the model scaling factor, k, is likely related to the fraction of ionizing photons that leak into the WIM; thus, k probably varies from H II region to H II region depending on the environment.

It is thus not surprising that the bottom panels of Figure 7 show clearly that Luisi et al. (2020) models with k- and m-parameter values derived for the W43 complex do not account for the WIM RRL intensities seen toward G20 and G45. The model intensities are too high by factors of $\sim$4 and $\sim$2, respectively, for G20 and G45. These sight lines were purposely chosen *not* to thread through environments even remotely like those found in massive star-forming regions such as W43.

Finally, it is clear from Figure 7 that the $\sim$115 km s^{-1} component toward G20 cannot be due to H II region leakage radiation. No nearby H II region is sufficiently bright or has a sufficiently narrow line width to explain this feature, as demonstrated by the Luisi et al. (2020) models and Appendix Table C1. We conclude it to be unlikely that this feature is due to extended ionized gas halos around H II regions. It may instead constitute a heretofore unrecognized phase of the WIM (see Section 5.1). To make further progress in the exploration of the nature of plasma halos around H II regions and this narrow RRL feature, we will need sensitive RRL maps of the WIM surrounding G20 and G45. Such maps will allow us to *fit* Luisi et al. (2020)–type models to these data.

3.6. Galactic ISM Context

Here, we assess the Galactic context of our G20 and G45 sight lines by comparing spectra for all phases of ISM hydrogen: H^+, H I, and H_2. This is done in Figure 8, which shows, for each sight line, spectra for $\langle \mathrm{Hn}\alpha \rangle$, 21 cm H I, and ^{13}CO(1→0), which is a proxy for H_2. These spectra were taken by different telescopes over a large range of frequencies, so their beam sizes sample different LOS volumes. The $\langle \mathrm{Hn}\alpha \rangle$ WIM RRL spectra have an HPBW of 2.′35. For G20, the H I spectrum is from the HI4PI all sky survey (HI4PI Collaboration et al. 2016; HPBW = 16.′2). The G45 H I spectrum stems from the Boston University–Arecibo Observatory H I survey

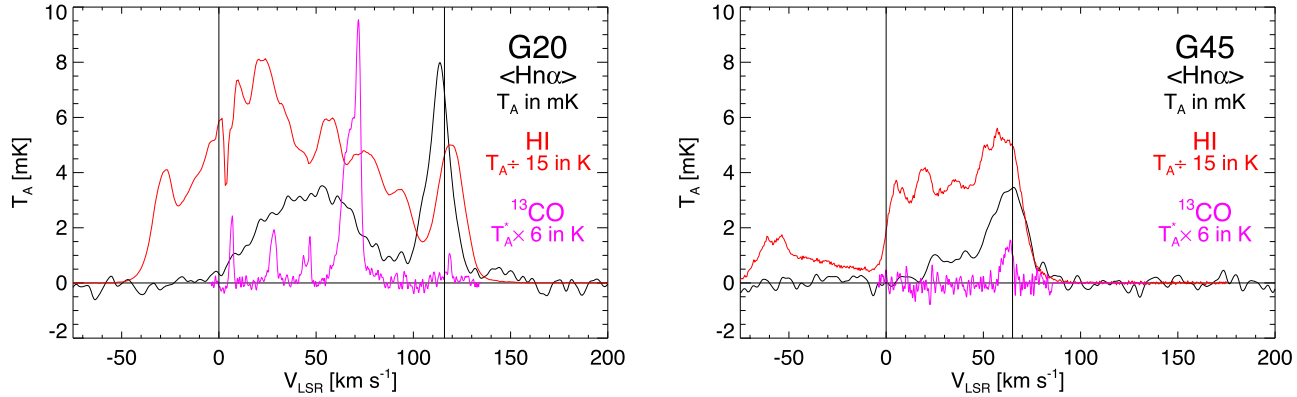

Figure 8. Spectra toward G20 and G45 showing all phases of gaseous interstellar hydrogen: $\langle \mathrm{Hn}\alpha \rangle$ H I, and ^{13}CO (a tracer of H_2). For clarity, the H I antenna temperatures in K are divided by a factor of 15, and the ^{13}CO T_A^* antenna temperatures in K are multiplied by a factor of 6. Vertical flags mark LSR velocities 0 km s^{-1} and the terminal velocity, V_T.

(Kuchar 1992; HPBW = 3′.2). The ^{13}CO spectra come from the Boston University–Five College Radio Observatory ^{13}CO Galactic Ring Survey (Jackson et al. 2006; HPBW = 42″). Despite their different angular resolutions, comparing these spectra can nonetheless provide useful insights. For example, the terminal velocity, V_T, flagged in Figure 8 is calculated for each sight line using the Clemens (1985) rotation curve. For both sight lines, the H^+, H I, and ^{13}CO spectra all have emission components at or near the terminal velocity.

Our sight lines probe two important loci in the first quadrant of the Galaxy. Some key properties of these sight lines, based on an assumed Sun to Galactic Center distance, R_0, of 8.5 kpc, are summarized in Table 4. (Other choices for R_0 would not alter the conclusions we reach here anent the spatial distribution of the WIM plasma.) Listed in Table 4 for each LOS are the minimum Galactocentric radius, $R_{\rm min} = R_0 \sin(\ell)$, tangent point distance from the Sun, $d_{\rm TP} = R_0 \cos(\ell)$, and total path length inside the solar orbit about the Galactic Center (GC), $d_{\rm LOS} = 2R_0 \cos(\ell)$.

Atomic hydrogen gas is ubiquitously distributed throughout the Galactic ISM. Because of this, for any LOS, 21 cm H I spectra show emission at all LSR velocities permitted by Galactic rotation. The velocity span of these H I spectra defines the maximum velocity spread permitted by Galactic rotation. For our first quadrant targets, gas at negative velocities is located in the Outer Galaxy beyond the solar orbit about the Galactic Center. The Figure 8 H I spectra have emission at negative LSR velocities that extends to ~ -50 km s^{-1} and ~ -75 km s^{-1} for G20 and G45, respectively. In contrast, neither of our target sight lines shows any $\langle \mathrm{Hn}\alpha \rangle$ RRL emission at negative LSR velocities at the sensitivity level achieved here. G20 shows $\langle \mathrm{Hn}\alpha \rangle$ emission at all velocities between 0 km s^{-1} and the terminal velocity, whereas G45 only shows RRL emission between $\sim +20$ km s^{-1} and the terminal velocity. Assuming perfect circular rotation and no streaming motions, all of the RRL emitting gas we see toward G20 and G45 must therefore be located in the Inner Galaxy, inside the solar orbit. This plasma must reside somewhere along the LOS paths, $d_{\rm LOS}$, summarized in Table 4.

Unlike H I, molecular gas in the Milky Way is found in comparatively dense, discrete clouds. This means that H_2/CO spectra will not have molecular emission spanning all available LSR velocities. As Figure 8 clearly shows, the molecular gas seen toward our target directions is concentrated into a few discrete emission components. At the sensitivity of the GRS,

Table 4
LOS Properties

LOS	$R_{\rm min}$ (kpc)	$d_{\rm TP}$ (kpc)	$d_{\rm LOS}$ (kpc)
G20	2.9	8.0	16.0
G45	6.0	6.0	12.0

Note. $R_0 = 8.5$ kpc.

G20 shows five molecular clouds and G45 has but one. For both sight lines, there are ^{13}CO emission components that match the LSR velocities of the highest-velocity RRL components in the $\langle \mathrm{Hn}\alpha \rangle$ spectra, albeit the ~ 114 km s^{-1} G20 ^{13}CO component is extremely weak. The GRS spectrometer could not detect emission at negative LSR velocities so these ^{13}CO spectra provide no Outer Galaxy information about molecular clouds toward these sight lines.

Cold H I embedded in a molecular cloud produces the absorption dips seen in the G20 H I spectrum at $V_{\rm LSR} = \sim 5$, ~ 50, and ~ 70 km s^{-1}. These H I dips are matched by ^{13}CO emission components. We suspect that all of the ^{13}CO components produce H I absorption but cannot definitively prove this due to a combination of mismatched angular resolution, insufficient spectral sensitivity, and the complex structure of Galactic H I spectra.

4. WIM RRL Emission Models

Here, using the $\langle \mathrm{Hn}\alpha \rangle$ emission seen from our targets, we seek to derive constraints on the LOS density and temperature distributions of the RRL emitting plasmas. Complete details of the modeling are provided in Appendix D. Models for RRL emission from LOS plasmas must specify the electron density, n_e, temperature, T_e, and velocity dispersion, σ, at every point along the $d_{\rm LOS}$. Each model comprises one or more plasma "clouds" distributed along the LOS. All clouds are homogeneous, isothermal plasmas in LTE. Each cloud's properties are specified at input. A cloud is defined by: location along the LOS, $d_\odot$, LOS path length size (a.k.a. the cloud diameter), $d_{\rm cloud}$, electron density, electron temperature, and velocity dispersion. We use the numerical code described in Appendix D to compute synthetic spectra for H109α RRL emission from the model plasmas. After these model $T_B(V_{\rm LSR})$ RRL spectra are calculated, we compare them to $\langle \mathrm{Hn}\alpha \rangle$ spectra

Table 5
LOS Tangent Point Models

LOS	Model	R_{gal} (kpc)	$d_{\odot}$ (kpc)	d_{cloud} (kpc)	n_e (cm^{-3})	T_e (K)	σ (km s^{-1})	EM (cm^{-6} pc)	p/k (cm^{-3} K)
G20	A	2.9	8.0	2.0	0.38	4000	5.7	289	1520
	B	2.9	8.0	2.0	0.29	2800	5.7	168	812
	rms	2.9	8.0	16.0	0.15	4000	5.7	360	600
G45	A	6.0	6.0	4.0	0.40	9000	8.6	640	3600
	B	6.0	6.0	4.0	0.31	6400	8.6	384	1984
	rms	6.0	6.0	12.0	0.18	9000	8.6	389	1620

that are converted to brightness temperature and smoothed to 5 km s^{-1} resolution.

We emphasize that the models are only intended to provide estimates of these quantities so we do not attempt to fully explore a large grid of parameter choices. Moreover, we do not apply any rigorous numerical metric to evaluate the "goodness of fit" between a model and the $\langle \mathrm{Hn}\alpha \rangle$ spectrum. We judge a model's fit by eye because we can only set limits on the electron temperature.

From the observed V_{LSR} span of these spectra we know, assuming circular rotation, that the RRL emitting plasma must be located within the solar orbit. The simplest assumption is that a constant-density isothermal plasma fills the entire d_{LOS} in each sight line (see Table 4). For this case, the observed EM provides an estimate for the rms electron density, n_e^{rms}:

$$n_e^{rms} = \left(\frac{EM}{d_{los}} \right)^{1/2}. \quad (7)$$

Table 2 shows that the total EM from the G20 and G45 emission components is 369.3 and 402.7 cm^{-6} pc, respectively. This gives from Equation (7) an n_e^{rms} of 0.15 and 0.18 cm^{-3}, respectively, for these sight lines. These n_e^{rms} estimates, however, do not account for gas clumping: there may be significant gaps and/or n_e density fluctuations in the plasma distribution along each LOS. Many different LOS n_e distributions can produce identical n_e^{rms} values.

Due to the first Galactic quadrant distance ambiguity, we cannot know a priori where the RRL emitting plasma is located vis a vis the LOS near/far locations. A series of models seeking to find cloud parameters that produce a synthetic spectrum matching the $\langle \mathrm{Hn}\alpha \rangle$ observations confirms that there is no unique solution. A plethora of models can reproduce the $\langle \mathrm{Hn}\alpha \rangle$ spectra. Because of this, models for our target's emission at LSR velocities having LOS distance ambiguities provide no meaningful limits for the plasma density and distribution along the LOS.

4.1. LOS Tangent Point Models

Models for RRL emitting gas located at the LOS tangent point distance, however, can provide useful constraints for the plasma physical properties. Gas is unambiguously located at the tangent point if it is emitting at the LSR terminal velocity produced by Galactic rotation for a particular first quadrant sight line. The high-velocity components seen toward G20 and G45 emit at their terminal velocities and are hence located at their respective tangent point distances from the Sun.

We model the RRL emission from these components using a single cloud each for G20 and G45. Each plasma cloud is specified by its LOS distance, $d_{\odot}$, cloud size, electron density, n_e, electron temperature, T_e, and the velocity dispersion of the emission component, σ. Each cloud is located at the tangent point distance (see Table 4). The velocity dispersion is set by the observed line width (see Table 2 where $\sigma = \Delta V/2.355$ for a Gaussian line shape).

We use the observed RRL line width, ΔV, to set the model plasma electron temperature. This line width stems from a combination of mechanisms including thermal, ΔV_{th}, and nonthermal broadening, ΔV_{nt}. In addition, velocity shear along the LOS produced by Galactic rotation, $dV_{LSR}/dd_{\odot}$, can also broaden the line emission, ΔV_{los}. (Quantum mechanical natural broadening is insignificant compared with these mechanisms.) The broadening processes add in quadrature to produce the observed line width: $\Delta V^2 = \Delta V_{th}^2 + \Delta V_{nt}^2 + \Delta V_{los}^2$. By definition, the LOS LSR velocity gradient at any Galactic tangent point distance, d_{TP}, is $dV_{LSR}/dd_{TP} = 0$. Thus, for plasma located at the tangent point, spectral broadening due to Galactic rotation, ΔV_{los}, is negligible. The WIM plasma is turbulent, however, so even at the tangent point, the observed RRL line width is an unknown combination of thermal and nonthermal, supersonic turbulent broadening: $\Delta V^2 = \Delta V_{th}^2 + \Delta V_{nt}^2$.

We estimate T_e in two ways, leading to two models each for G20 and G45. Model A sets T_e to be the upper limit derived using Equation (4) and assuming that ΔV_{obs} is entirely due to thermal broadening: $\Delta V = \Delta V_{th}$. Because the plasma is turbulent, this is a robust upper limit for T_e. For Model A, T_e is 4000 K and 9000 K for G20 and G45, respectively. Model B explores the effect of turbulent broadening by assuming that the thermal and turbulent contributions to the line width are equal: $\Delta V_{th} = \Delta V_{nt}$. The thermal contribution to the observed line width is then $\Delta V_{th} = \Delta V/\sqrt{2}$. For Model B, T_e is 2800 K and 6400 K for G20, and G45, respectively.

Here, we seek to reproduce both the intensity and line shape of the tangent point emission components. The model cloud parameters that are yet to be determined are the electron density and cloud size. For an isothermal plasma, the RRL intensity scales linearly with emission measure so $T_B \propto n_e^2$. The model spectral intensities are very sensitive to n_e. We find that changing n_e by ± 0.01 cm^{-3} produces significant differences in the model peak T_B intensity. The cloud size is constrained by the line shape: if the cloud is too large, Galactic rotation produces a distinctly non-Gaussian line profile.

To craft the final model parameters, we explored a range of choices for n_e and d_{cloud}. The models are summarized in Table 5, which lists for each cloud the minimum LOS Galactocentric distance, R_{gal}, location along the LOS, $d_{\odot}$, LOS path length size (i.e., the cloud diameter), d_{cloud}, electron density, n_e, electron temperature, T_e, velocity dispersion, σ, emission measure, EM, and the plasma pressure, p/k. The Model A spectra for G20 and G45 are compared in Figure 9 with the observed $\langle \mathrm{Hn}\alpha \rangle$ emission. The Model B spectra are

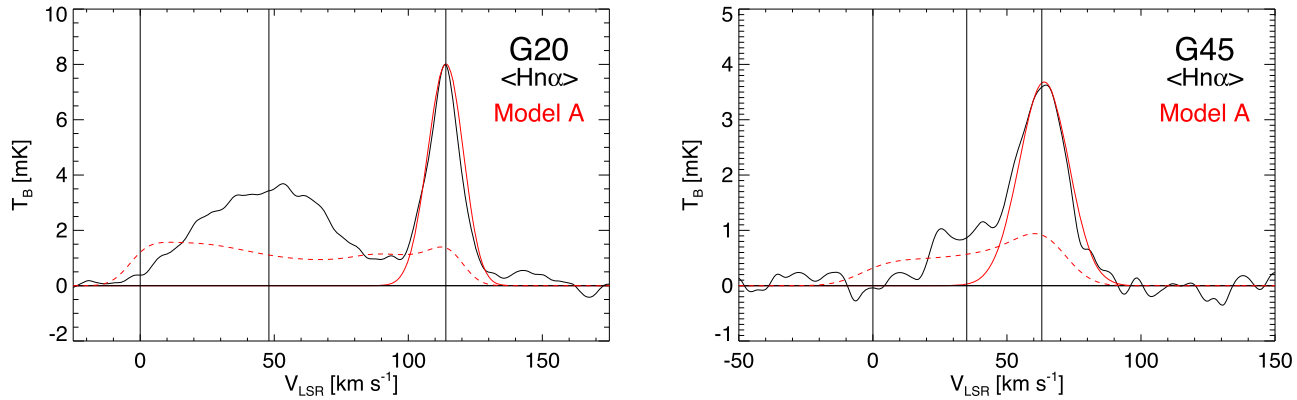

Figure 9. LTE models for RRL emission (solid red curves) from the G20 and G45 high-velocity components compared with the observed $\langle \mathrm{Hn}\alpha \rangle$ brightness temperature spectrum (black curves). Properties of the models are summarized in Table 5. Vertical lines flag LSR velocities at 0 km s^{-1} and the observed component velocities listed in Table 2. Model B is not shown because it is indistinguishable from Model A. The dashed red curve models have plasma filling the entire LOS inside the solar orbit with the rms density from Equation (7).

not shown because their n_e has been adjusted to fit the observed $\langle \mathrm{Hn}\alpha \rangle$ and so they are indistinguishable from Model A.

The dashed red curve models in Figure 9 have plasma filling the entire LOS inside the solar orbit with the rms electron density from Equation (7) (see Model "rms" in Table 5). As expected, these models are poor fits to the observed $\langle \mathrm{Hn}\alpha \rangle$ spectra because the plasma is surely not homogeneous and isothermal throughout the d_{LOS} path length. The models do, however, show the LSR velocity span produced by plasma that fills the entire d_{LOS}. For both sight lines, these models produce larger intensities for V_{LSR}'s between ~ 0 and ~ 20 km s^{-1} than what is observed. This may indicate that the plasma density is rather low near the Sun for both directions.

5. Discussion

Here, we compare our results for G20 and G45 with other studies of the WIM. This is challenging because there is no universally accepted definition of the WIM. The plasma has been investigated using a variety of spectral observations over a range of frequencies. The WIM has been studied in the optical, far-infrared (FIR), and radio. Interpreting these spectra requires many different techniques and assumptions before one derives physical properties such as density and temperature. Furthermore, because of dust extinction and differing angular resolutions, these three spectral regimes probe different volumes of the Milky Way.

Historically, the distribution and physical properties of the WIM in the Milky Way have primarily been characterized by observations of optical spectral lines. Hα emission studies conclude that the WIM accounts for ~90% of the ionized gas in the ISM with a scale height of ~1–2 kpc (e.g., Reynolds 1989; Hill et al. 2008). Dispersion measures from pulsars with known distances, together with Hα emission measures, estimate the range of the average electron density to be ~0.03–0.10 cm^{-3} with a filling factor, $f \sim 0.4$–0.2 (e.g., Reynolds 1991a; Taylor & Cordes 1993; Berkhuijsen et al. 2006; Gaensler et al. 2008). The ratio of [N II] λ5755 and [N II] λ6583 provides a direct measure of the electron temperature and indicates the WIM is about 2000 K warmer than H II regions (Reynolds et al. 2001). For a typical H II region with $T_e = 8000$ K, this corresponds to an electron temperature of 10^4 K.

Most of the ionized gas in the Milky Way, however, is located in the Inner Galaxy, which is not probed by optical emission lines because of extinction by dust. FIR collisionally excited lines are less affected by dust and offer an alternative method to sample the WIM. In particular, [N II] 122 μm and [N II] 205 μm are excellent diagnostics of the WIM since nitrogen has an ionization potential of 14.5 eV, similar to hydrogen (13.6 eV), and will thus be associated with H II.

Using the HIFI instrument on Herschel, Persson et al. (2014) observed [N II] 205 μm toward four H II regions. They detected absorption of [N II] from foreground gas toward W31C and W49N. This absorbing gas must be located within the solar orbit due to the velocity range of the spectral components. Assuming an N/H abundance ratio and filling factor, they estimate mean electron densities of ~0.1–0.3 cm^{-3}. These results, together with modeling of N^+ with RADEX, are consistent with the optically derived WIM properties, albeit with somewhat higher electron densities.

Observations of RRLs offer an extinction-free probe of the WIM. Early RRL observations made with single-dish telescopes toward directions away from OB-type-star excited H II regions detected weak RRL emission (e.g., Gottesman & Gordon 1970; Lockman 1976; Mezger 1978; Heiles et al. 1996; Roshi & Anantharamaiah 2000). This emission was interpreted by Mezger (1978) as being associated with the envelopes of H II regions and called the "extended low density" (ELD) H II. Because of their poor angular resolution, however, all of these observations suffer from confusion with the known population of H II regions (Anderson et al. 2014), so any quantitative interpretation of these data is problematic.

The more recent RRL surveys with the GBT and FAST, however, have sufficient angular resolution to avoid emission from H II regions and in principle produce WIM-only images (Anderson et al. 2021). But there are several reasons why these WIM-only images may still contain ELD H II emission and thus not be truly representative of WIM gas: (1) GDIGS is only sensitive to plasmas with mean electron densities $\gtrsim$30 cm^{-3} (for a path length of 1 pc), and this is ~ 100 times larger than the density expected for the WIM (see the Figure 3 sensitivity comparison); (2) since Hα studies imply that the WIM fills ~70% of the ISM's volume, this semi-ubiquitously distributed plasma ought to emit over the entire range of velocities that are allowed by Galactic rotation, yet for typical sight lines, the GDIGS detected RRL spectra have gaps with no emission at allowed LSR velocities; and (3) the RRL emission appears to

be correlated with the location of H II regions (Luisi et al. 2020) and therefore may be part of the ELD H II.

For the high-sensitivity RRL observations toward G20 and G45, we estimate rms electron densities of $(n_e^2)^{1/2} \sim 0.15 - 0.18\ \mathrm{cm}^{-3}$ over a wide range of velocities. For a filling factor of $f = 0.3$, this corresponds to mean electron densities of $\sim 0.3\ \mathrm{cm}^{-3}$. These electron densities are somewhat higher than expected from the WIM based on optical data. These higher values may not be surprising since Figure 7 suggests that some of the emission detected toward both G20 and G25 might be associated with OB-type star H II regions. But the Figure also shows that the G20 RRL emission above 100 $\mathrm{km\,s}^{-1}$ and the G45 emission below 50 $\mathrm{km\,s}^{-1}$ have no association with any nearby H II regions and are probably tracing the WIM.

5.1. G20

The narrow, 13.5 $\mathrm{km\,s}^{-1}$, line width from plasma located at the G20 tangent point distance sets a strong upper limit of $\lesssim$4,000 K on the electron temperature. At this T_e, Model A with a density of $n_e = 0.38\ \mathrm{cm}^{-3}$ replicates the observed intensity and line shape of this emission component. The Model A $p/k = n_e T_e$ pressure is $\lesssim 1520\ \mathrm{cm}^{-3}$ K. Models A and B together span n_e between ~ 0.38–$0.29\ \mathrm{cm}^{-3}$ and T_e between $\sim$ 4000–2800 K resulting in WIM pressures ranging from $p/k \sim 1500$–$800\ \mathrm{cm}^{-3}$ K.

Measuring the pressure in the WIM is challenging because there do not seem to be any observables from which one can derive both the density and temperature without bias. Combining the pulsar/H91α density determinations with the FIR derived electron temperature yields a nominal pressure, p/k, of ~ 500–$1000\ \mathrm{cm}^{-3}$ K for the WIM plasma. But combining these n_e and T_e determinations may be problematic. For example, these estimates for the WIM plasma's physical parameters are not probing the same gas volumes. In lieu of robust observational constraints for the WIM p/k, we can seek insight from simulations. The TIGRESS-NCR simulation of the Galactic ISM (Kim et al. 2023) predicts a WIM pressure p/k ranging between $\sim 10^2$ and $\sim 10^5$, with a mean value close to $\sim 10^4\ \mathrm{cm}^{-3}$ K.

Here, we show that a combination of RRL observations with models for the emission together provide an alternative approach to deriving the WIM pressure. Using the observed RRL line width to constrain T_e and models to estimate n_e, we find that the p/k pressure derived here for the G20 tangent point emission is generally consistent with other determinations of the WIM pressure that are based on observations. The low T_e limit, however, is not. Too, the electron density is at the high end for values typically derived for WIM plasma. Altogether, the G20 model for the tangent point emission challenges our understanding of the WIM as a canonically pervasive, low-density, $\lesssim 0.1\ \mathrm{cm}^{-3}$, $\sim$ 10,000 K plasma.

5.2. G45

The line width, 20.3 $\mathrm{km\,s}^{-1}$, for the G45 tangent point emission component also sets a strong upper limit for the plasma electron temperature of $T_e \lesssim 9000$ K. Model A adopts this T_e limit and with a density of $n_e = 0.40\ \mathrm{cm}^{-3}$ replicates the observed intensity and line shape of this emission component. Models A and B together span n_e between ~ 0.40–$0.31\ \mathrm{cm}^{-3}$ and T_e between $\sim$ 9000–6400 K resulting in WIM pressures ranging from $p/k \sim 3600$–$2000\ \mathrm{cm}^{-3}$ K.

These model p/k pressures are also consistent with other determinations of the WIM pressure and are more in line with the TIGRESS-NCR simulation results. Again, the density is at the high end of values reported for the WIM, but overall this G45 tangent point emission component's physical properties are consistent with WIM plasma.

In sum, the result of these efforts is that the WIM spans a range of densities. Almost any density up to a $\sim$few cm^{-3} may be consistent with the WIM. Optical studies derive $n_e \sim 0.03$–$0.1\ \mathrm{cm}^{-3}$(Haffner et al. 2009). FIR observations of fine structure transitions infer ~ 0.1–$0.3\ \mathrm{cm}^{-3}$(Persson et al. 2014). Our G20 and G45 analysis gives ~ 0.3–$0.4\ \mathrm{cm}^{-3}$. Finally, there is evidence from low-frequency RRL observations for a more-or-less continuous distribution of plasma densities. Several studies have found volume filling factors inversely proportional to density, so the higher densities subsume an increasingly smaller fraction of the ISM volume (e.g., Anantharamaiah 1985, 1986; Roshi & Anantharamaiah 2001).

6. Summary

Studies of the Milky Way's WIM that use Hα emission can only probe the Galactic disk out to distances limited to a few kiloparsecs from the Sun due to extinction. Because the ISM is optically thin at centimeter wavelengths, radio recombination lines probe the WIM emission at transgalactic path lengths. Here, we use RRL emission to study two Galactic sight lines located in the plane that are devoid of any OB-star produced H II regions and show no indication of nearby star formation.

1. GBT observations of the WIM made toward Galactic sight lines G20 and G45 show four Gaussian-shaped emission features in the $\langle \mathrm{Hn}\alpha \rangle$ stacked RRL spectra. The emission measures of these spectral components range between $\sim$100 and $\sim 300\ \mathrm{cm}^{-6}$ pc.
2. For both sight lines, RRL emission can be seen at nearly all LSR velocities between 0 $\mathrm{km\,s}^{-1}$ and the terminal velocity produced by Galactic rotation. The lack of any significant RRL emission at LSR velocities below 0 $\mathrm{km\,s}^{-1}$ means that in these directions, RRL emission from any WIM plasma located beyond the solar orbit is below the EM $\gtrsim 10\ \mathrm{cm}^{-6}$ pc (3σ limit for 5 $\mathrm{km\,s}^{-1}$ resolution) sensitivity limit of our GBT observations. For G20 and G45, the LOS path lengths with RRL emitting WIM plasma, d_{LOS}, must thus be no larger than 16 and 12 kpc, respectively.
3. The observed $\langle \mathrm{Hn}\beta \rangle / \langle \mathrm{Hn}\alpha \rangle$ intensity ratios are consistent with LTE excitation for the stronger, higher-velocity components seen toward both sight lines at LSR velocities of $\sim$113 $\mathrm{km\,s}^{-1}$ and $\sim$63 $\mathrm{km\,s}^{-1}$ for G20 and G45, respectively. The weaker, lower-velocity components at $\sim$48 $\mathrm{km\,s}^{-1}$ and $\sim$35 $\mathrm{km\,s}^{-1}$, however, show some evidence for non-LTE excitation.
4. Although our sight lines show no H II regions in their fields, the WIM emission we observe might originate in extended WIM halos around H II regions. Some of the emission detected toward both G20 and G45 occurs at LSR velocities shared with nearby H II regions. Empirical models for WIM emission near H II regions predict comparable emission to what is seen (see Figure 7), although the model uncertainties preclude us from making any definitive conclusions. Despite these uncertainties, it seems unlikely that the G20 RRL emission

above 100 km s^{-1} is associated with nearby known H II regions.

5. Cloud models with plasma located at the G20 and G45 tangent points reproduce the observed RRL emission components at the tangent point velocities for these sight lines. These models have densities $n_e = \sim$0.29–0.40 cm^{-3}, temperatures $T_e = \sim$2800–9000 K, and p/k pressures $\sim$ 800–3600 cm^{-3} K.
6. The p/k pressure derived for the G20 tangent point emission is consistent with other determinations of the WIM pressure. The low, $\lesssim$4000 K T_e limit, however, is not. The G20 model for the tangent point emission challenges our understanding of the WIM as a canonically pervasive, low-density, $\lesssim$0.1 cm^{-3}, $\sim$ 10,000 K plasma.

Acknowledgments

We dedicate this paper to the memory of Ron Reynolds who pioneered the modern study of the Milky Way's WIM. Ron commented on an early version of this manuscript. We thank the referee for a timely and close reading of our manuscript. We thank the GBT telescope operators whose diligence and expertise in executing our observing scripts for project GBT/20A–483 were exceptional. The Green Bank Telescope is operated by the Green Bank Observatory (GBO). The GBO and the National Radio Astronomy Observatory (NRAO) are facilities of the National Science Foundation (NSF) operated under cooperative agreements by Associated Universities, Inc. This publication makes use of data products from the Wide-field Infrared Survey Explorer, which is a joint project of the University of California, Los Angeles, and the Jet Propulsion Laboratory/California Institute of Technology, funded by the National Aeronautics and Space Administration. This research was supported by NSF awards AST-1714688 to T.M.B. and AST-1516021 to L.D.A. T.V.W. is supported by the AST-2202340 NSF Astronomy and Astrophysics Postdoctoral Fellowship.

Facility: GBT.

Software: `TMBIDL` (Bania et al. 2016).

Appendix A
RRL Transitions Used for Stacked Spectra

Instrumental effects caused by the *C*-band receiver, the GBT IF system, and VEGAS spectrometer compromise some of the transitions we observe. These effects include unacceptable frequency structure in the spectral baselines and loss of sensitivity due to high system temperatures. High system temperatures mostly occur when the *C*-band receiver performance deteriorates at both the high- and low-frequency extremes of the $\sim$4 GHz bandwidth. We inspected each RRL tuning to evaluate overall quality. The usable RRL transitions are summarized in Table A1. Listed for the G20 and G45 targets are the transition, the rest frequency, and the average system temperatures for both linear polarizations: $\langle T_{XX} \rangle$ and $\langle T_{YY} \rangle$. For these acceptable tunings, system temperatures typically range between $\sim$20 K and $\sim$40 K.

Table A1
RRL Transitions Used for Stacked Spectra

Line	Transition $n+\Delta n \rightarrow n$	Frequency (GHz)	$\langle T_{XX}\rangle_{G20}$ (K)	$\langle T_{YY}\rangle_{G20}$ (K)	$\langle T_{XX}\rangle_{G45}$ (K)	$\langle T_{YY}\rangle_{G45}$ (K)
H97α	98 → 97	7.09541	38.6	38.3	38.0	37.4
H98α	99 → 98	6.88149	35.4	33.4	34.6	31.9
H99α	100 → 99	6.67607	35.8	27.6	35.1	26.5
H100α	101 → 100	6.47876	24.6	25.1	23.9	24.1
H101α	102 → 101	6.28914	29.8	21.1	28.5	20.2
H102α	103 → 102	6.10685	28.5	21.7	27.6	20.8
H103α	104 → 103	5.93154	26.9	22.8	25.8	21.8
H104α	105 → 104	5.76288	24.2	23.4	23.0	22.4
H105α	106 → 105	5.60055	23.8	24.0	22.5	22.8
H106α	107 → 106	5.44426	21.2	24.2	20.1	23.1
H107α	108 → 107	5.29373	27.1	23.7	25.6	22.5
H108α	109 → 108	5.14870	24.6	26.4	23.1	25.1
H109α	110 → 109	5.00892	25.8	24.1	24.0	22.8
H110α	111 → 110	4.87416	26.0	24.0	24.2	22.8
H111α	112 → 111	4.74418	27.0	23.7	24.9	22.5
H112α	113 → 112	4.61879	27.1	25.2	25.2	24.0
H114α	115 → 114	4.38095	30.2	32.4	27.6	30.7
H115α	116 → 115	4.26814	38.9	39.1	36.0	36.0
H122β	124 → 122	7.06872	34.1	35.0	33.3	34.8
H123β	125 → 123	6.89905	34.6	32.9	33.7	31.8
H124β	126 → 124	6.73479	34.0	31.3	33.1	29.9
H125β	127 → 125	6.57570	27.7	26.4	26.7	25.1
H126β	128 → 126	6.42158	24.5	29.8	23.7	28.6
H127β	129 → 127	6.27223	30.3	22.4	29.2	21.4
H128β	130 → 128	6.12748	31.0	22.2	29.4	21.2
H129β	131 → 129	5.98714	28.8	22.5	27.6	21.5
H130β	132 → 130	5.85107	25.5	22.6	24.3	21.5
H131β	133 → 131	5.71909	24.3	23.1	23.1	21.9
H132β	134 → 132	5.59105	24.3	23.9	23.2	22.8
H133β	135 → 133	5.46680	22.5	23.3	21.2	22.0
H134β	136 → 134	5.34619	21.7	25.7	20.5	24.3
H135β	137 → 135	5.22913	25.6	17.3	23.8	16.3
H136β	138 → 136	5.11544	26.4	22.9	24.8	21.8
H137β	139 → 137	5.00502	25.4	24.1	23.8	22.8
H138β	140 → 138	4.89778	25.9	24.2	24.0	23.0
H139β	141 → 139	4.79357	26.3	23.7	24.4	22.5
H140β	142 → 140	4.69229	28.2	24.8	25.9	23.3
H141β	143 → 141	4.59384	30.0	23.5	27.5	22.2
H143β	145 → 143	4.40508	29.9	30.5	27.4	28.7
H145β	147 → 145	4.22650	42.4	32.8	38.3	30.8
H139γ	142 → 139	7.11476	40.8	42.4	39.9	41.4
H140γ	143 → 140	6.96495	34.1	32.3	33.5	31.5
H141γ	144 → 141	6.81933	38.5	32.8	37.5	31.6
H143γ	146 → 143	6.54004	26.5	26.2	25.6	25.1
H144γ	147 → 144	6.40609	23.2	28.7	22.5	27.6
H146γ	149 → 146	6.14898	23.9	23.5	22.9	22.4
H147γ	150 → 147	6.02558	27.6	23.2	26.4	22.2

Appendix B
Radio Recombination Line Excitation Analysis

B.1. LTE Excitation

Are the $\langle$Hn$\alpha\rangle$, $\langle$Hn$\beta\rangle$, and $\langle$Hn$\gamma\rangle$ stacked spectra consistent with LTE excitation? To make this assessment, we need to know the expected LTE ratio between a specific $n+\Delta n \rightarrow n$ transition and a fiducial $n+1 \rightarrow n$ transition. Here, we use $\langle$Hn$\alpha\rangle$ as the fiducial transition and calculate the LTE ratios expected for $\langle$Hn$\beta\rangle$ and $\langle$Hn$\gamma\rangle$. First we calculate the statistical weights, g_n, and oscillator strengths, $f_{n+\Delta n,n}$, for each RRL transition listed in Appendix Table A1. Since these transitions were used to craft the stacked spectra, we use the average statistical weight, $\langle g_n\rangle$, and average oscillator strength, $\langle f_{n+\Delta n,n}\rangle$, for $\langle$Hn$\alpha\rangle$, $\langle$Hn$\beta\rangle$, and $\langle$Hn$\gamma\rangle$ to derive the expected LTE ratios.

The quantum properties of the Table A1 transitions are compiled in Table B1. Listed are the transition, the principle quantum number, n, the order of the transition, Δn, the statistical weight, g_n, and oscillator strength, $f_{n+\Delta\, n,n}$. The statistical weight is $g_n = 2 \times n^2$, and we use the prescription in Menzel (1968) to derive the oscillator strengths, $f_{n+\Delta n,n}$, for recombination transitions between principle quantum numbers $n+\Delta n \rightarrow n$.

Table B1
Oscillator Strengths

Transition	n	Δn	g_n	$f_{n+\Delta n,n}$
H97α	97	1	18818	18.79132765
H98α	98	1	19208	18.98210255
H99α	99	1	19602	19.17287745
H100α	100	1	20000	19.36365235
H101α	101	1	20402	19.55442725
H102α	102	1	20808	19.74520215
H103α	103	1	21208	19.93597705
H104α	104	1	21632	20.12675195
H105α	105	1	22050	20.31752685
H106α	106	1	22472	20.50830175
H107α	107	1	22898	20.69907665
H108α	108	1	23328	20.88985155
H109α	109	1	23762	21.08062645
H110α	110	1	24200	21.27140135
H111α	111	1	24642	21.46217625
H112α	112	1	25088	21.65295115
H114α	114	1	25992	22.03450095
H115α	115	1	26450	22.22527585
H122β	122	2	29768	3.29151250
H123β	123	2	30258	3.31784460
H124β	124	2	30752	3.34417670
H125β	125	2	31250	3.37050880
H126β	126	2	31752	3.39684090
H127β	127	2	32258	3.42317300
H128β	128	2	32768	3.44950510
H129β	129	2	33282	3.47583720
H130β	130	2	33800	3.50216930
H131β	131	2	34322	3.52850140
H132β	132	2	34848	3.55483350
H133β	133	2	35378	3.58116560
H134β	134	2	35912	3.60749770
H135β	135	2	36450	3.63382980
H136β	136	2	36992	3.66016190
H137β	137	2	37538	3.68649400
H138β	138	2	38088	3.71282610
H139β	139	2	38642	3.73915820
H140β	140	2	39200	3.76549030
H141β	141	2	39762	3.79182240
H143β	143	2	40898	3.84448660
H145β	145	2	42050	3.89715080
H139γ	139	3	38642	1.16315647
H140γ	140	3	39200	1.17126209
H141γ	141	3	39762	1.17936771
H143γ	143	3	40898	1.19557895
H144γ	144	3	41472	1.20368457
H146γ	146	3	42632	1.21989581
H147γ	147	3	43218	1.22800143

The LTE RRL intensity ratio between two optically thin transitions is given by the ratio of their oscillator strengths, $f_{n+\Delta\,n,n}/f'_{n+\Delta\,n,n}$, and their statistical weights, g_n/g'_n:

$$\text{LTE Intensity Ratio} = \frac{\langle g_n\rangle \times \langle f_{n+\Delta\,n,n}\rangle}{\langle g_n^{'}\rangle \times \langle f_{n+\Delta\,n,n}^{'}\rangle}. \tag{B1}$$

Here, $\langle f'_{n+\Delta\,n,n}\rangle$ and $\langle g'_n\rangle$ refer to the fiducial transition, $\langle \text{Hn}\alpha\rangle$, and the angle brackets denote the average of the quantum properties of the transitions used to derive the stacked spectra. The average quantum properties for the $\langle \text{Hn}\alpha\rangle$, $\langle \text{Hn}\beta\rangle$, and $\langle \text{Hn}\gamma\rangle$ stacked spectra are summarized in Table B2, which lists $\langle g_n\rangle$, $\langle f_{n+\Delta\,n,n}\rangle$, and $\langle g_n\rangle \times \langle f_{n+\Delta\,n,n}\rangle$. The last column of Table B2 gives the LTE intensity ratios for $\langle \text{Hn}\beta\rangle$ and $\langle \text{Hn}\gamma\rangle$ relative to $\langle \text{Hn}\alpha\rangle$.

The "LTE?" column in Table 3 gives the ratio between the observed RRL transition ratios and the expected LTE ratio. In LTE this ratio of ratios would be unity. For the strongest WIM components—113.4 km s^{-1} for G20 and 63.3 km s^{-1} for G45—this ratio is 1.11 ± 0.11 and 1.08 ± 0.11, respectively. We thus find that, within the errors, our $\langle \text{Hn}\beta\rangle/\langle \text{Hn}\alpha\rangle$ ratios are consistent with LTE excitation for both sight lines.

The lower-velocity components in these directions, however, give values for the "LTE?" parameter that are significantly larger than one: 1.34 ± 0.13 and 1.95 ± 0.34 for G20 and G45, respectively. Moreover, all ratios involving the $\langle \text{Hn}\gamma\rangle$ spectra are compromised by the much poorer sensitivity of these spectra due to their comparatively small integration times compared with the $\langle \text{Hn}\alpha\rangle$ and $\langle \text{Hn}\beta\rangle$ data. These $\langle \text{Hn}\gamma\rangle$ spectra can only provide upper limits, and these limits are not significant.

B.2. Non-LTE Excitation

We thus find that the $\langle \text{Hn}\beta\rangle$ lower-velocity components seen in the G20 and G45 spectra show some evidence for non-LTE excitation in the WIM gas. These non-LTE effects can be described by the use of departure coefficients, b_n. Departure coefficients relate the true level population, N_n, to the population level under LTE, N_n^*, where $b_\text{n} = (N_\text{n}/N_\text{n}^*)$. Non-LTE effects can alter the RRL intensities in the following way (see Equation (14.52) in Wilson et al. 2009):

$$\frac{T_\text{L}}{T_\text{L}^*} = b_\text{n}\left(1 - \frac{1}{2}\,\tau_\text{c}\,\beta_\text{n}\right), \tag{B2}$$

where T_L is the observed line intensity, T_L^* is the LTE intensity, and τ_c is the continuum optical depth. Here, β_n is a measure of the gradient of b_n with respect to n (see Equation (14.40) in Wilson et al. 2009):

$$\beta_\text{n} = 1 - 20.836\left(\frac{T_\text{e}}{\text{K}}\right)\left(\frac{\nu}{\text{GHz}}\right)^{-1}\left(\frac{d\,\ln b_\text{n}}{d\,\text{n}}\right)\Delta\, n. \tag{B3}$$

The first term in Equation (B2) accounts for the effect of non-LTE line formation whereas the second describes non-LTE line transfer effects, which can include maser amplification of the line radiation. When β becomes negative, $\beta_\text{n} < 0$, maser amplification occurs, and the resulting RRL intensities will depend on radiative transfer details.

For the low densities expected in the WIM, however, the continuum opacity should be small at centimeter wavelengths, and thus $\tau_\text{c} \ll 1$. The main non-LTE effect will therefore be departures in the level populations, and so the non-LTE line intensity is the LTE intensity times b_n: $T_\text{L} = b_\text{n}\, T_\text{L}^*$.

As the principle quantum number $n \rightarrow \infty$, b_n approaches unity. Since n increases with Δn for RRLs at the same frequency (e.g., H102α, H129β, and H147γ have nearly identical rest frequencies), we expect the Hnβ transitions to be closer to LTE than the Hnα transitions. The observed $\langle \text{Hn}\beta\rangle$ intensities should thus be larger than expected when in LTE, consistent with the results in Figure 6 and Table 3.

In sum, we find that for the strongest WIM components seen in G20 and G45 the $\langle \text{Hn}\beta\rangle/\langle \text{Hn}\alpha\rangle$ ratios are consistent with LTE excitation. The weaker components, however, show some evidence for non-LTE excitation. The $\langle \text{Hn}\alpha\rangle$ intensity can be weaker than the LTE value because collisions are less effective

Table B2
Average Quantum Properties and LTE Ratio

Transition	$\langle g_n \rangle$	$\langle f_{n+\Delta n,n} \rangle$	$\langle g_n \rangle \times \langle f_{n+\Delta n,n} \rangle$	LTE Ratio
$\langle \mathrm{Hn}\alpha \rangle$	22365.000	20.43411151	4.5700890395e+05	1.00000
$\langle \mathrm{Hn}\beta \rangle$	35271.273	3.57159029	1.2597453522e+05	0.27565
$\langle \mathrm{Hn}\gamma \rangle$	40832.000	1.19442100	4.8770598447e+04	0.10672

Note. Average quantum properties from Table B1. LTE intensity ratio relative to $\langle \mathrm{Hn}\alpha \rangle$ from Equation (B1).

due the size of the H atom compared with the larger size of the nearby (in frequency) $\langle \mathrm{Hn}\beta \rangle$ transition. For the larger $\langle \mathrm{Hn}\beta \rangle$ atom collisions are more effective in establishing LTE level populations, and the deviation from LTE is smaller. As a consequence, the $\langle \mathrm{Hn}\beta \rangle / \langle \mathrm{Hn}\alpha \rangle$ ratio can exceed the LTE value.

Appendix C
H II Regions Located near the G20 and G45 Sight Lines

Properties of WISE Catalog H II regions located within 100′ of the G20 and G45 sight lines are compiled in Table C1. Listed for each nebula are the galactic coordinates, (ℓ, b), and angular separation from the sight line, together with the IR radius, R_{IR}, RRL intensity, T_L, LSR velocity, V_{LSR}, FWHM line width, ΔV, and their measurement errors. Some of the entries in the WISE Catalog refer to nebulae that reside within the same telescope beam. In those cases, the Catalog lists identical V_{LSR} and ΔV values (see Anderson et al. 2014). When such confusion within the beam occurs, we only list here (and use in Figure 7) a single nebula, choosing the one with the smallest separation from its fiducial sight line. Some WISE H II region spectra have emission at multiple velocities. Because we have no reason to choose otherwise, in these cases, we plot all of the velocities in Figure 7.

Table C1
H II Regions Near G20 and G45

H II Region	Separation (arcmin)	R_{IR} (arcmin)	ℓ (deg)	b (deg)	T_L (mK)	σ_T (mK)	V_{LSR} (km s^{-1})	σ_{LSR} (km s^{-1})	ΔV (km s^{-1})	$\sigma_{\Delta V}$ (km s^{-1})
G020.098−00.123	9.44	0.7	20.10	−0.123	32.3	0.3	43.4	0.1	20.3	0.2
G020.083−00.135	9.48	0.5	20.08	−0.134	31.0	2.8	42.2	1.4	31.7	3.3
G019.818+00.010	10.92	1.9	19.82	+0.010	26.1	0.4	60.4	0.1	18.2	0.3
G020.227+00.110	15.13	1.2	20.23	+0.110	10.5	0.2	22.1	0.2	14.9	0.4
G019.728−00.113	17.67	0.7	19.73	−0.113	15.4	0.4	57.3	0.3	21.7	0.7
G019.677−00.134	20.96	1.0	19.68	−0.133	48.0	5.8	55.0	1.2	20.0	2.8
G019.780+00.286	21.65	1.9	19.78	+0.287	21.3	0.3	−9.3	0.2	21.7	0.4
G020.363−00.014	21.80	0.7	20.36	−0.014	21.8	0.5	54.1	0.2	16.6	0.4
G020.150−00.335	22.03	9.4	20.15	−0.335	19.0	2.9	67.3	1.5	20.3	3.6
G019.741+00.280	22.89	0.7	19.74	+0.280	32.2	0.4	16.3	0.1	25.5	0.3
G019.629−00.095	22.96	5.5	19.63	−0.094	54.0	3.7	58.6	0.8	22.8	1.8
G019.716−00.261	23.11	1.0	19.72	−0.261	29.6	0.5	40.1	0.1	15.2	0.3
G019.675−00.226	23.69	3.5	19.68	−0.225	168.5	1.7	42.5	0.1	26.5	0.4
G019.594+00.024	24.40	0.7	19.59	+0.024	12.8	0.3	35.3	0.4	29.0	1.0
G019.666−00.309	27.25	1.2	19.67	−0.308	33.9	0.8	44.3	0.2	19.2	0.5
G019.609−00.239	27.46	1.4	19.61	−0.238	168.5	1.7	42.5	0.1	26.5	0.4
G020.457+00.021	27.48	1.7	20.46	+0.022	66.7	1.1	73.8	0.1	15.0	0.3
G019.554−00.248	30.60	3.2	19.55	−0.248	131.0	7.4	41.0	0.8	27.7	1.8
G020.481+00.168	30.63	2.6	20.48	+0.169	24.0	2.3	24.1	1.0	20.5	2.2
G019.494−00.150	31.65	1.9	19.49	−0.149	34.3	0.4	32.1	0.1	16.8	0.3
G019.494−00.150	31.65	1.9	19.49	−0.149	20.5	0.4	54.6	0.2	15.1	0.5
G019.489+00.135	31.68	0.9	19.49	+0.135	56.0	3.4	19.8	0.5	17.5	1.2
G019.504−00.193	31.88	0.9	19.50	−0.193	45.4	0.4	37.8	0.1	19.9	0.2
G019.466+00.168	33.58	4.8	19.47	+0.168	45.0	0.5	109.3	0.1	23.2	0.3
G019.466+00.168	33.58	4.8	19.47	+0.168	145.0	0.6	19.9	0.0	14.9	0.1
G019.466+00.168	33.58	4.8	19.47	+0.168	8.2	0.6	70.8	0.6	16.3	1.4
G020.542−00.179	34.24	3.0	20.54	−0.179	40.5	0.6	48.6	0.1	16.2	0.3
G020.576+00.103	35.13	1.6	20.58	+0.104	12.8	0.3	28.8	0.3	25.2	0.9
G020.728−00.105	44.18	6.6	20.73	−0.104	141.0	0.5	56.0	0.0	26.5	0.1
G020.727−00.259	46.34	4.1	20.73	−0.259	97.8	0.3	55.2	0.0	20.4	0.1
G019.122−00.263	54.94	1.1	19.12	−0.262	32.3	0.4	56.0	0.2	35.3	0.5
G019.122−00.263	54.94	1.1	19.12	−0.262	27.2	0.5	100.4	0.2	18.1	0.4
G019.064−00.282	58.63	1.3	19.06	−0.282	164.8	1.8	64.4	0.1	25.2	0.3
G019.604−00.905	59.24	1.0	19.60	−0.905	...	...	38.7	1.2	36.7	2.8
G020.988+00.092	59.54	2.2	20.99	+0.092	47.0	5.6	18.6	1.3	21.4	2.9
G021.004−00.056	60.33	0.7	21.00	−0.056	18.0	0.2	28.8	0.1	19.6	0.3
G018.978+00.030	61.35	4.6	18.98	+0.031	26.0	2.5	52.3	1.7	36.1	3.9
G019.030+00.423	63.47	1.3	19.03	+0.424	8.1	0.8	25.4	0.7	14.8	1.6
G020.966−00.455	64.10	15.4	20.97	−0.455	10.0	1.1	38.5	2.5	45.5	6.0
G019.045−00.588	67.27	2.0	19.05	−0.588	36.0	3.7	68.2	1.0	18.6	2.2
G018.914−00.329	68.08	12.9	18.91	−0.329	217.9	0.8	68.0	0.1	23.8	0.1
G018.914−00.329	68.08	12.9	18.91	−0.329	12.5	1.1	36.2	0.6	14.3	1.5
G018.832−00.300	72.35	0.7	18.83	−0.300	46.1	0.4	46.4	0.1	30.0	0.3
G018.881−00.493	73.37	1.8	18.88	−0.493	92.0	5.3	65.5	0.8	27.1	1.8
G018.725−00.046	76.52	12.5	18.73	−0.045	22.0	2.4	63.5	2.4	45.4	6.0
G018.741+00.250	77.01	1.1	18.74	+0.251	29.1	0.5	19.1	0.2	22.1	0.5
G018.710+00.000	77.36	0.8	18.71	+0.000	16.6	0.3	31.8	0.3	44.5	0.8
G018.677−00.236	80.63	1.2	18.68	−0.236	57.0	11.3	42.6	0.6	23.2	1.3
G018.657−00.057	80.64	1.4	18.66	−0.056	...	...	44.1	0.9	32.4	2.2
G018.750−00.535	81.57	1.1	18.75	−0.535	18.5	0.6	66.5	0.4	25.9	1.0
G018.632+00.256	83.49	1.1	18.63	+0.256	22.8	0.7	18.4	0.2	12.9	0.4
G018.630+00.309	84.26	0.7	18.63	+0.309	25.3	0.4	14.0	0.1	17.5	0.3
G021.386−00.255	84.54	1.0	21.39	−0.254	...	...	92.1	1.1	32.3	2.7
G018.594+00.321	86.51	3.1	18.59	+0.322	44.3	0.2	13.4	0.0	17.1	0.1
G018.631−00.492	87.23	3.2	18.63	−0.492	31.2	0.2	61.6	0.1	30.3	0.2
G018.584+00.344	87.43	0.7	18.58	+0.344	28.0	0.6	10.8	0.2	16.7	0.4
G021.426−00.546	91.64	1.0	21.43	−0.546	...	...	70.2	0.6	25.3	1.8
G018.461−00.003	92.33	0.5	18.46	−0.003	...	...	56.5	0.4	30.3	1.0
G021.560−00.108	93.84	2.9	21.56	−0.108	24.9	0.3	115.1	0.2	23.0	0.5
G021.450−00.590	93.95	2.0	21.45	−0.590	38.3	0.3	72.7	0.1	20.5	0.2
G021.603−00.169	96.72	0.5	21.60	−0.169	8.2	0.4	−4.7	0.6	23.0	1.5
G021.634−00.003	98.05	1.9	21.63	−0.002	24.5	0.3	20.2	0.1	19.8	0.3
G045.070+00.132	8.99	1.0	45.07	+0.132	...	...	59.2	0.8	24.8	2.1

Table C1
(Continued)

H II Region	Separation (arcmin)	R_{IR} (arcmin)	ℓ (deg)	b (deg)	T_L (mK)	σ_T (mK)	V_{LSR} (km s^{-1})	σ_{LSR} (km s^{-1})	ΔV (km s^{-1})	$\sigma_{\Delta V}$ (km s^{-1})
G045.121+00.133	10.83	1.7	45.12	+0.133	...	...	56.7	0.5	44.5	1.6
G045.453+00.044	27.31	4.1	45.45	+0.045	742.9	1.6	54.2	0.0	27.6	0.1
G045.195−00.439	28.82	1.3	45.20	−0.439	18.9	0.4	72.9	0.2	25.1	0.6
G045.475+00.130	29.55	2.4	45.48	+0.130	...	...	55.6	0.1	29.5	0.3
G044.552−00.239	30.42	3.8	44.55	−0.239	12.8	0.4	58.4	0.2	13.6	0.5
G044.811−00.492	31.59	4.6	44.81	−0.492	17.0	2.5	44.8	4.0	30.0	5.5
G045.542−00.006	32.52	0.7	45.54	−0.006	42.3	0.3	55.0	0.1	26.2	0.2
G044.501+00.332	35.97	0.8	44.50	+0.332	48.5	0.2	−43.0	0.1	22.0	0.1
G045.002−00.611	36.62	5.8	45.00	−0.610	8.7	0.3	61.3	0.4	24.6	0.9
G044.521+00.385	36.87	0.7	44.52	+0.385	18.1	0.2	−49.7	0.1	25.9	0.3
G044.375−00.076	37.76	4.2	44.38	−0.076	11.4	0.1	56.7	0.1	33.5	0.3
G045.634−00.016	38.08	1.8	45.63	−0.016	3.6	0.2	9.2	0.6	19.6	1.6
G044.689−00.579	39.42	2.1	44.69	−0.579	6.8	0.2	41.9	0.4	19.6	0.9
G044.379−00.327	42.11	5.0	44.38	−0.327	22.8	0.5	61.1	0.2	18.6	0.5
G045.503+00.495	42.38	1.9	45.50	+0.496	7.4	0.4	−35.9	0.7	23.8	1.9
G045.689−00.235	43.70	4.0	45.69	−0.235	8.4	0.3	19.1	0.5	34.0	1.3
G044.904−00.733	44.30	2.2	44.90	−0.732	15.7	0.3	65.6	0.2	17.2	0.4
G045.197+00.740	45.96	1.3	45.20	+0.740	18.7	0.2	−35.0	0.2	31.4	0.4
G044.224+00.085	46.79	5.3	44.22	+0.085	21.0	2.8	59.6	3.4	30.4	4.7
G044.418+00.535	47.43	1.4	44.42	+0.536	13.1	0.2	−55.1	0.2	25.0	0.4
G045.391−00.725	49.39	3.2	45.39	−0.724	53.0	0.5	52.5	0.1	20.6	0.2
G045.773−00.378	51.62	1.4	45.77	−0.377	11.7	0.6	51.0	0.4	15.1	0.9
G045.825−00.291	52.47	1.2	45.83	−0.290	...	...	61.2	0.2	26.3	0.5
G045.882−00.088	53.23	4.8	45.88	−0.087	13.2	0.1	62.4	0.1	19.1	0.2
G045.882−00.088	53.23	4.8	45.88	−0.087	2.2	0.1	18.2	0.5	28.9	1.3
G044.094−00.015	54.31	1.8	44.09	−0.014	12.6	0.3	66.6	0.3	23.6	0.8
G045.933−00.403	60.98	1.0	45.93	−0.402	...	...	63.9	0.5	21.1	1.3
G046.033−00.097	62.28	3.1	46.03	−0.096	8.0	0.1	63.5	0.2	28.5	0.6
G044.331−00.837	64.26	2.8	44.33	−0.837	13.9	0.4	62.5	0.2	17.0	0.6
G046.069+00.216	65.47	1.1	46.07	+0.216	6.2	0.3	12.4	0.4	17.6	0.9
G046.088+00.254	67.05	0.4	46.09	+0.255	7.6	0.3	13.4	0.4	17.0	0.9
G043.894+00.197	67.37	2.8	43.89	+0.198	5.7	0.2	−38.1	0.4	21.3	1.0
G043.794−00.129	72.74	0.6	43.79	−0.129	...	...	43.3	1.1	31.9	3.0
G043.774+00.057	73.64	2.5	43.77	+0.058	33.1	0.3	70.5	0.1	20.8	0.2
G043.818+00.395	74.78	1.8	43.82	+0.395	29.6	0.2	−10.5	0.1	27.6	0.2
G043.730+00.114	76.49	2.1	43.73	+0.115	8.3	0.3	73.1	0.4	22.4	0.9
G046.173+00.533	77.36	1.0	46.17	+0.533	10.2	0.2	6.3	0.2	24.8	0.6
G046.203+00.532	78.95	0.7	46.20	+0.532	5.5	0.2	4.6	0.6	29.9	1.4
G046.213+00.547	79.88	0.6	46.21	+0.548	5.5	0.2	5.8	0.6	26.3	1.3
G043.890−00.780	81.40	1.0	43.89	−0.780	...	...	53.4	0.4	28.4	1.0
G043.999+00.978	83.97	2.3	44.00	+0.979	4.4	0.2	−17.1	0.6	25.4	1.5
G043.968+00.993	85.92	0.8	43.97	+0.993	11.1	0.5	−21.6	0.6	23.8	1.5
G046.495−00.241	90.85	5.0	46.49	−0.240	257.8	1.1	57.7	0.0	18.3	0.1
G043.523−00.648	96.75	1.5	43.52	−0.648	4.4	0.4	55.4	1.1	26.8	2.7
G043.432+00.516	99.04	1.2	43.43	+0.517	22.5	0.3	−12.8	0.2	22.7	0.3

Appendix D
Numerical Modeling of RRL Emission from WIM Plasmas

Models for WIM RRL emission from LOS plasmas must specify the plasma electron density, n_e, temperature, T_e, and velocity dispersion, σ, at every point along the d_{LOS}. We use a numerical code to craft synthetic RRL emission spectra for G20 and G45. `TMBIDL` already includes code, `MODEL_HI`, that calculates 21 cm H I spectra for any Galactic LOS direction and distribution of physical properties. The radiative transfer calculation is one-dimensional: the LOS is modeled as a series of slabs of thickness, dx, with some total LOS path length. The LOS can have any arbitrary distribution of density, excitation temperature, and velocity dispersion.

We modified the `TMBIDL MODEL_HI` code to calculate instead the LOS radiative transfer for a pure hydrogen plasma in LTE. The models compute spectra for the H109α transition, whose 5.00 GHz rest frequency is the average for the $\langle$Hn$\alpha\rangle$ spectra. We follow the Balser et al. (2021) technique. Assuming the Rayleigh–Jeans limit, $h\nu \ll kT_e$, the brightness temperature as a function of frequency, ν, is given by

$$T_B(\nu) = T_e(1 - e^{-\tau_L(\nu)}), \quad \text{(D1)}$$

where $\tau_L(\nu)$ is the optical depth, $\tau_L(\nu) = \int \kappa_L(\nu)\, d\ell$, and T_e is the plasma electron temperature. Here $\kappa_L(\nu)$ is the absorption coefficient, and $d\ell$ is the path length through the ionized gas.

The RRL absorption coefficient (Condon & Ransom 2016) is:

$$\kappa_{\rm L}(\nu) = \frac{c^2}{8\pi\nu_{\rm L}^2}\frac{g_{\rm u}}{g_{\rm l}} n_{\rm l} A_{\rm ul}\left[1 - \exp\left(-\frac{h\nu_{\rm L}}{kT_{\rm e}}\right)\right]\phi(\nu), \quad \text{(D2)}$$

where c is the speed of light, $\nu_{\rm L}$ is the frequency of the RRL transition, $(g_{\rm u}/g_{\rm l})$ is the ratio of statistical weights for the upper and lower levels, $n_{\rm l}$ is the number density in the lower state, $A_{\rm ul}$ is the spontaneous emission rate from the upper to lower state, h is Planck's constant, k is Boltzmann's constant, and $\phi(\nu)$ is the normalized line shape. The statistical weights for hydrogen are $g_{\rm n} = 2n^2$. The spontaneous emission rate from the upper to the lower state, $A_{\rm ul}$, can be approximated (Condon & Ransom 2016) as:

$$A_{\rm n+1,n} = \left(\frac{64\pi^6 m_{\rm e} e^{10}}{3c^3h^6}\right)\frac{1}{n^5}, \quad \text{(D3)}$$

where $m_{\rm e}$ is the electron mass, e is the electric charge, and n is the principal quantum number. We assume a Gaussian line profile, $\phi(\nu)$:

$$\phi(\nu) = \frac{1}{\sqrt{2\pi\sigma^2}}\exp\left[-\frac{(\nu-\nu_{\rm L})^2}{2\sigma^2}\right]. \quad \text{(D4)}$$

In order to compare model $T_{\rm B}(\nu)$ spectra with the $\langle {\rm Hn}\alpha\rangle$ observations, we must calculate a $T_{\rm B}(V_{\rm LSR})$ model spectrum. To do this, each slab must be assigned an LSR velocity derived from the Galactic LOS direction, ℓ, location along the LOS, $d_\odot$, and an assumed Galactic rotation curve model. Once this $V_{\rm LSR}$ vs $d_\odot$ relation is established, we use the Doppler equation at the H109α rest frequency to transform $T_{\rm B}(\nu)$ to $T_{\rm B}(V_{\rm LSR})$. `TMBIDL` has several Galactic rotation curve choices available. The conclusions we reach here about the WIM do not depend on the choice of any particular rotation curve. Here, for all of our models, we adopt the Clemens (1985) rotation curve scaled to $R_0 = 8.5$ kpc.

Each model comprises one or more plasma "clouds" distributed along the LOS. All clouds are homogeneous, isothermal, and in LTE. Each cloud's properties are specified at input. A cloud is defined by: location along the LOS, $d_\odot$, LOS path length size (a.k.a. the cloud diameter), $d_{\rm cloud}$, electron density, $n_{\rm e}$, plasma electron temperature, $T_{\rm e}$, and velocity dispersion, σ.

ORCID iDs

T. M. Bania https://orcid.org/0000-0003-4866-460X
Dana S. Balser https://orcid.org/0000-0002-2465-7803
Trey V. Wenger https://orcid.org/0000-0003-0640-7787
Spencer J. Ireland https://orcid.org/0000-0002-9449-2485
L. D. Anderson https://orcid.org/0000-0001-8800-1793
Matteo Luisi https://orcid.org/0000-0001-8061-216X

References

Anantharamaiah, K. R. 1985, JApA, 6, 203
Anantharamaiah, K. R. 1986, JApA, 7, 131
Anderson, L. D., Bania, T. M., Balser, D. S., et al. 2014, ApJS, 212, 1
Anderson, L. D., Deharveng, L., Zavagno, A., et al. 2015, ApJ, 800, 101
Anderson, L. D., Luisi, M., Liu, B., et al. 2021, ApJS, 254, 28
Balser, D. S. 2006, AJ, 132, 2326
Balser, D. S., Roshi, D. A., Jeyakumar, S., et al. 2016, ApJ, 816, 22
Balser, D. S., Wenger, T. V., Anderson, L. D., et al. 2021, ApJ, 921, 176
Bania, T., Wenger, T., Balser, D., & Anderson, L., 2016 TMBIDL: Single dish radio astronomy data reduction package, Astrophysics Source Code Library, ascl:1605.005
Belfiore, F., Santoro, F., Groves, B., et al. 2022, A&A, 659, A26
Berkhuijsen, E. M., Mitra, D., & Mueller, P. 2006, AN, 327, 82
Clemens, D. P. 1985, ApJ, 295, 422
Condon, J. J., & Ransom, S. M. 2016, Essential Radio Astronomy (Princeton, NJ: Princeton Univ. Press)
Dennison, B., Simonetti, J. H., & Topasna, G. A. 1998, PASA, 15, 147
Dettmar, R. J. 1990, A&A, 232, L15
Ellis, G. R. A., Waterworth, M. D., & Bessell, M. 1962, Natur, 196, 1079
Gaensler, B. M., Madsen, G. J., Chatterjee, S., & Mao, S. A. 2008, PASA, 25, 184
Gaustad, J. E., McCullough, P. R., Rosing, W., & Van Buren, D. 2001, PASP, 113, 1326
Ghigo, F., Maddalena, R., Balser, D., & Langston, G. 2001, GBT Commissioning Memo: Gain and Efficiency at S-Band, GBT Commissioning Memo No. 10
Gordon, M. A., & Sorochenko, R. L. 2002, Radio Recombination Lines. Their Physics and Astronomical Applications, Vol. 282 (Dordrecht: Kluwer)
Gottesman, S. T., & Gordon, M. A. 1970, ApJL, 162, L93
Haffner, L. M., Dettmar, R. J., Beckman, J. E., et al. 2009, RvMP, 81, 969
Haffner, L. M., Reynolds, R. J., Tufte, S. L., et al. 2003, ApJS, 149, 405
Heiles, C., Reach, W. T., & Koo, B.-C. 1996, ApJ, 466, 191
HI4PI Collaboration, Ben Bekhti, N., Flöer, L., et al. 2016, A&A, 594, A116
Hill, A. S., Benjamin, R. A., Kowal, G., et al. 2008, ApJ, 686, 363
Hou, L., Han, J., Hong, T., Gao, X., & Wang, C. 2022, SCPMA, 65, 129703
Hoyle, F., & Ellis, G. R. A. 1963, AuJPh, 16, 1
Jackson, J. M., Rathborne, J. M., Shah, R. Y., et al. 2006, ApJS, 163, 145
Kim, C.-G., Kim, J.-G., Gong, M., & Ostriker, E. C. 2023, ApJ, 946, 3
Kuchar, T. A. 1992, PhD thesis, Boston Univ., Massachusetts
Lockman, F. J. 1976, ApJ, 209, 429
Luisi, M., Anderson, L. D., Balser, D. S., Bania, T. M., & Wenger, T. V. 2016, ApJ, 824, 125
Luisi, M., Anderson, L. D., Liu, B., Anish Roshi, D., & Churchwell, E. 2019, ApJS, 241, 2
Luisi, M., Anderson, L. D., Liu, B., et al. 2020, ApJ, 889, 96
Maddalena, R. 2010, Theoretical Ratio of Beam Efficiency to Aperture Efficiency, GBT Memo No. 276
Menzel, D. H. 1968, Natur, 218, 756
Mezger, P. G. 1978, A&A, 70, 565
Ott, M., Witzel, A., Quirrenbach, A., et al. 1994, A&A, 284, 331
Peng, B., Kraus, A., Krichbaum, T. P., & Witzel, A. 2000, A&AS, 145, 1
Persson, C. M., Gerin, M., Mookerjea, B., et al. 2014, A&A, 568, A37
Rand, R. J., Kulkarni, S. R., & Hester, J. J. 1990, ApJL, 352, L1
Reber, G., & Ellis, G. R. 1956, JGR, 61, 1
Reynolds, R. J. 1989, ApJL, 339, L29
Reynolds, R. J. 1991a, ApJL, 372, L17
Reynolds, R. J. 1991b, in IAU Symp. 144, The Interstellar Disk-Halo Connection in Galaxies, ed. H. Bloemen (Dordrecht: Kluwer), 67
Reynolds, R. J., Scherb, F., & Roesler, F. L. 1973, ApJL, 181, L79
Reynolds, R. J., Sterling, N. C., Haffner, L. M., & Tufte, S. L. 2001, ApJL, 548, L221
Reynolds, R. J., & Tufte, S. L. 1995, ApJL, 439, L17
Roshi, D. A., & Anantharamaiah, K. R. 2000, ApJ, 535, 231
Roshi, D. A., & Anantharamaiah, K. R. 2001, ApJ, 557, 226
Roshi, D. A., Balser, D. S., Bania, T. M., Goss, W. M., & De Pree, C. G. 2005, ApJ, 625, 181
Tanenbaum, B. S., Zeissig, G. A., & Drake, F. D. 1968, Sci, 160, 760
Taylor, J. H., & Cordes, J. M. 1993, ApJ, 411, 674
Wenger, T. V., Balser, D. S., Anderson, L. D., & Bania, T. M. 2019, ApJ, 887, 114
Wilson, T. L., Rohlfs, K., & Hüttemeister, S. 2009, Tools of Radio Astronomy (Berlin: Springer)
Wood, K., & Mathis, J. S. 2004, MNRAS, 353, 1126
Wright, E. L., Eisenhardt, P. R. M., Mainzer, A. K., et al. 2010, AJ, 140, 1868